Boundary-Phase Control of Sequentially Addressed Trapped-Ion ZZ Interactions

Chun-Yang Luan[1,2,*], Haiyu Ding[1,2], Cheng-Kang Pan[1,2], Xiangjie Li[1,2], Lin Cheng[1,2], Gangxi Wang[1,2], Yuting Lei[1,2], Peilin Zheng[1,2], Shixin Hu[1,2], Xiang Zhang[4,5,*], and Fei Wang[1,2,*]

[1]Future Research Lab, China Mobile Research Institute, Beijing 100053, China
[2]Beijing Key Laboratory of Quantum and AI Integration Technology, Beijing 100053, China
[4]Department of Physics, Renmin University of China, Beijing 100872, China
[5]Beijing Key Laboratory of Opto-electronic Functional Materials and Micro-nano Devices, Renmin University of China, Beijing 100872, China

*Correspondence: chunyangluan@163.com; siang.zhang@ruc.edu.cn; wangfei@chinamobile.com

Supplementary Information

S1. Model Scope

This Supplementary Information provides the derivations, numerical settings, convergence tests, control grids, and source-data descriptions supporting the main text. The analysis combines a representative reduced model, physical Coulomb-chain modes, zero-overlap waveform synthesis, reduced-spin channels, many-ion transfer tests, and robustness scans.

Unless stated otherwise, all numerical values are obtained from the simulation models defined below. We use *interaction* for Hamiltonian coupling, *ZZ phase-generation primitive* for phase accumulation without requiring complete motional closure, and *gate* only when the reduced spin channel and local corrections are evaluated.

S2. Derivation of the Reduced Boundary-Phase Hamiltonian from the 435 nm E2 Light Shift

S2.1 Qubit basis and state-dependent light shift

For the representative $^{171}\mathrm{Yb}^+$ clock-state encoding,

$$|0\rangle = |^2S_{1/2}, F=0, m_F=0\rangle, \qquad |1\rangle = |^2S_{1/2}, F=1, m_F=0\rangle, \tag{S1}$$

and $\sigma_j^z = |1\rangle_j\langle 1| - |0\rangle_j\langle 0|$. The implementation reported in Ref. [1] uses two non-copropagating 435 nm fields near the narrow, dipole-forbidden $^2S_{1/2} \leftrightarrow {}^2D_{3/2}$ electric-quadrupole transition. Its qubit-selective optical coupling acts on the $F=1, m_F=0$ clock component through the $D_{3/2}, F=1, m_F=\pm 1$ states, while the other clock component is far from resonance. Writing $|e_\tau\rangle = |^2D_{3/2}, F=1, m_F=\tau\rangle$ for $\tau=\pm 1$, the rotating optical interaction has the form reported in Ref. [1],

$$H_{E2}(t) = \hbar \sum_{j,\tau=\pm 1} \left[g_{Aj}^{\tau}(t) e^{-i(\boldsymbol{k}_A\cdot\hat{\boldsymbol{r}}_j + \pi\mu t + \phi_{Aj})} + g_{Bj}^{\tau}(t) e^{-i(\boldsymbol{k}_B\cdot\hat{\boldsymbol{r}}_j - \pi\mu t + \phi_{Bj})} \right] |e_\tau\rangle_j\langle 1| + \mathrm{h.c.} \tag{S2}$$

The matrix elements are E2 couplings and therefore depend on both field polarization and wave vector. Under the symmetric-detuning and polarization conditions of the primary reference, excited-manifold elimination yields a traveling projector-type light shift

$$H_{\mathrm{LS}}(t) = \hbar \sum_j \chi_j(t) P_{1j} \sin[\Delta\boldsymbol{k}\cdot(\boldsymbol{r}_j^0 + \hat{\boldsymbol{q}}_j) - 2\pi\mu t - \phi_j(t)], \tag{S3}$$

where $P_{1j} = |1\rangle_j\langle 1| = (\mathbb{I}+\sigma_j^z)/2$, $\Delta\boldsymbol{k} = \boldsymbol{k}_A - \boldsymbol{k}_B$, and ϕ_j is the relative beat-note phase at ion j. The ordinary beat frequency μ is stored in hertz, while χ_j is an angular-frequency light-shift amplitude. The amplitude selected by the acousto-optic deflector (AOD) is parameterized as

$$\chi_j(t) = \bar{\chi} f(t) s_j(t), \tag{S4}$$

where $s_j(t)$ includes the intended addressing window, finite rise/fall, dark intervals, and explicitly configured leakage. The phase programmed by the direct digital synthesizer (DDS) can be decomposed as

$$\phi_j(t) = \phi_{\mathrm{DDS},j}(t) + \phi_{\mathrm{AOD},j}(t) + \phi_{\mathrm{opt},j}, \tag{S5}$$

where $\phi_{\mathrm{opt},j}$ is a relative optical-path or standing-wave offset, not a common absolute optical-carrier phase. Decomposing P_{1j} separates a scalar force from the differential σ_j^z force. Scalar–scalar commutators give only a global phase, scalar–spin commutators give local Z phases, and spin–spin commutators give the pairwise ZZ term. The reduced model includes the spin–spin component and treats the local terms through echo or frame calibration.

S2.2 Motional expansion and Lamb–Dicke reduction

For radial motion along the force direction,

$$\hat{\boldsymbol{q}}_j = \sum_m \boldsymbol{e}_{jm}\sqrt{\frac{\hbar}{2M\omega_m}}(a_m + a_m^\dagger), \qquad \eta_{jm} = \Delta\boldsymbol{k}\cdot\boldsymbol{e}_{jm}\sqrt{\frac{\hbar}{2M\omega_m}}, \tag{S6}$$

so $\Delta\boldsymbol{k}\cdot\hat{\boldsymbol{q}}_j = \sum_m \eta_{jm}(a_m + a_m^\dagger)$. With $\Xi_j = \Delta\boldsymbol{k}\cdot\boldsymbol{r}_j^0 - 2\pi\mu t - \phi_j$,

$$\sin\left[\Xi_j + \sum_m \eta_{jm}(a_m + a_m^\dagger)\right] = \sin\Xi_j + \cos\Xi_j\sum_m \eta_{jm}(a_m + a_m^\dagger) + \mathcal{O}(\eta^2). \tag{S7}$$

The first-order expression requires $|\eta_{jm}|\sqrt{2\bar{n}_m + 1} \ll 1$ for all populated modes. The spin-differential reduction assumes that the zeroth-order differential Stark term is removed by an echo or tracked as a single-qubit frame; Section S2.7 restores it explicitly and states the conditions for that reduction. The first-order term is the spin-dependent force; its constant sine-to-cosine quadrature offset is absorbed into the phase origin.

S2.3 Motional interaction picture, force quadratures, and rotating-wave approximation

Under $U_m(t) = \exp[-i\sum_m \omega_m a_m^\dagger a_m t]$, $a_m \to a_m e^{-i\omega_m t}$, with $\omega_m = 2\pi\nu_m$. Terms at the sum frequency $\omega_m + 2\pi\mu$, off-resonant carrier-like terms, and other rapidly rotating components are discarded when their detunings exceed both the effective force rate and the envelope bandwidth. The real positive/negative-frequency force carrier used in the simulation is

$$c_j(t) = \frac{1}{2}\left[A_+\cos(\theta_j + \phi_+) + A_-\cos(\theta_j + \phi_-)\right]. \tag{S8}$$

The baseline balance condition $A_+ = A_- = 1$ and $\phi_+ = \phi_- = 0$ gives $c_j = \cos\theta_j$. These terms are positive- and negative-frequency force quadratures rather than an E1 Raman-sideband implementation. Departures from balance are treated as reduced-model calibration parameters.

The numerical configuration separates the nominal model prefactor from its scalar force calibration. We define

$$\Omega_F^{(\mathrm{eff})} \equiv f_{\mathrm{force}}\Omega_F^{(\mathrm{model})}, \tag{S9}$$

where $\Omega_F^{(\mathrm{model})}$ is stored in hertz and f_{force} is the dimensionless force scale reported by the calibrated schedules. The unadorned Ω_F in the implementation-independent main-text Hamiltonian denotes this effective prefactor.

The reduced real-force Hamiltonian is

$$H_I(t) = \hbar \sum_{j,m} g_{jm}(t)\sigma_j^z \left(a_m e^{-i\omega_m t} + a_m^\dagger e^{i\omega_m t}\right), \tag{S10}$$

with

$$g_{jm}(t) = 2\pi\Omega_F^{(\mathrm{eff})} f(t) s_j(t) \eta_{jm} c_j(t). \tag{S11}$$

The coefficient g_{jm} is real and has units of radians per second. The configuration stores both $\Omega_F^{(\mathrm{model})}$ and the derived $\Omega_F^{(\mathrm{eff})}$ in hertz, so the single conversion by 2π in Eq. (S11) is mandatory.

For a constant phase rate, the identity

$$\cos(2\pi\mu t + \varphi)e^{i\omega_m t} = \frac{1}{2}\left[e^{i(\omega_m+2\pi\mu)t+i\varphi} + e^{i(\omega_m-2\pi\mu)t-i\varphi}\right] \tag{S12}$$

shows explicitly how the real-force form separates into fast and slow quadratures. Dropping the sum-frequency term gives the detuning-frame RWA

$$H_I^{(\mathrm{RWA})}(t) = \hbar \sum_{j,m} \sigma_j^z \left[F_{jm}(t) a_m + F_{jm}^*(t) a_m^\dagger\right], \qquad F_{jm} = \frac{G_{jm}}{2} e^{i[\delta_{jm}t + \varphi_j(t)]}, \tag{S13}$$

where $G_{jm} = 2\pi\Omega_F^{(\mathrm{eff})} f s_j \eta_{jm}$ and

$$\delta_{jm} = 2\pi(\mu + \delta_j - \nu_m). \tag{S14}$$

The calculations use a detuning that is constant within each scan instance. For a time-dependent detuning, the phase $\delta_{jm}t$ in Eq. (S13) is replaced by $\int_0^t \delta_{jm}(t')dt'$. Thus δ_{jm} is drive minus mode. More generally, if $c_j = q_+ e^{i\theta_j} + q_+^* e^{-i\theta_j}$, then $F_{jm} = G_{jm} q_+ e^{i(\theta_j - \omega_m t)}$ and the balanced setting has $q_+ = 1/2$. The full real-force solver retains both this term and the counter-rotating term at $\omega_m + 2\pi(\mu + \delta_j)$; the two representations must not be multiplied together or applied sequentially.

S2.4 AOD/AOM compensation and the boundary-phase condition

The controller residual detuning is

$$\delta_j(t) = \Delta f_{\mathrm{AOD},j}(t) - \Delta f_{\mathrm{AOM},j}(t) + \delta_{\mathrm{res},j}(t), \tag{S15}$$

where every quantity on the right is stored in hertz. The operational inter-window phase reference is

$$\theta_j(t) = \theta_0 + \int_0^t 2\pi[\mu + \delta_j(t')]dt' + \phi_{\mathrm{DDS},j}(t) + \phi_{\mathrm{AOD},j}(t) + \phi_{\mathrm{opt},j}. \tag{S16}$$

Ideal upstream acousto-optic-modulator (AOM) compensation gives $\Delta f_{\mathrm{AOD},j} - \Delta f_{\mathrm{AOM},j} = 0$ in the sign convention used here. The explicit 2π in Eq. (S16) converts the stored beat frequency and residual detuning from hertz to radians per second before time integration. Equation (S16) describes the laboratory controller phase. In Eq. (S13), $\varphi_j(t)$ is the corresponding force-quadrature phase after the explicitly accumulated drive–mode detuning has been separated. These phases therefore describe the same controller evolution in different frames and are not added twice.

Three phases have distinct origins. The oscillator phase $\omega_m t$ is generated by free motional evolution. The RF/DDS phase-clock coherence coordinate $\theta_j(t)$ is generated by the programmed force frequency and DDS/AOD phase words; it fixes the force quadrature at a window boundary. The absolute optical-carrier phase is common to the eliminated optical oscillation and does not enter the light-shift force. A relative standing-wave or path phase remains observable through $\phi_{\mathrm{opt},j}$, but it is not the absolute carrier phase. Thus optical-carrier phase insensitivity is compatible with sensitivity to the programmed force-quadrature boundary phase. When $s_j(t) = 0$, the Hamiltonian vanishes even though the controller phase continues to advance.

S2.5 Magnus outputs and approximation boundary

For Eq. (S13), the first two Magnus terms give

$$\alpha_{jm}(T) = -i\int_0^T F_{jm}^*(t)dt, \tag{S17}$$

$$\Phi_{ij}(T) = -\sum_m \int_0^T dt_1 \int_0^{t_1} dt_2 \,\mathrm{Im}\big[F_{im}(t_1)F_{jm}^*(t_2) + F_{jm}(t_1)F_{im}^*(t_2)\big]\,. \tag{S18}$$

Same-ion terms are state independent because $(\sigma_j^z)^2 = 1$. The full real-force reference is recovered exactly by using $F_{jm}^{(\mathrm{full})} = g_{jm}^{(\mathrm{real})}e^{-i\omega_m t}$ in the same complex recurrence. The RWA instead uses Eq. (S13); their difference is the discarded sum-frequency quadrature, not a second force. For the baseline parameters, the numerical comparison gives a 2.01×10^{-5} absolute (2.83×10^{-4} relative) single-window displacement difference and a 1.39×10^{-7}-rad (2.78×10^{-5} relative) two-window phase difference between the full-real and RWA calculations. The exact full-real coefficient identity agrees to 1.39×10^{-17} rad in pair phase. The reduced model does not include multilevel spontaneous scattering or optical excited-state dynamics; Section S2.7 restores the deterministic common and differential projector coordinates.

S2.6 Finite-window proof for disjoint force windows

For one mode,

$$[F_a(t_1)a + F_a^*(t_1)a^\dagger, F_b(t_2)a + F_b^*(t_2)a^\dagger] = 2i\,\mathrm{Im}[F_a(t_1)F_b^*(t_2)]. \tag{S19}$$

Substitution into the ordered second Magnus term and collection of $(a,b) = (i,j)$ and (j,i) gives Eq. (S18) without an additional factor of two. Writing $F_{jm}(t) = \sum_p F_{jm}^{(p)}(t)\chi_{W_{jp}}(t)$ gives

$$\Phi_{ij} = \sum_m\sum_{p,q}\mathcal{K}_m^{ij}(W_{ip}, W_{jq}) + \mathcal{K}_m^{ji}(W_{jp}, W_{iq}), \tag{S20}$$

where

$$\mathcal{K}_m^{ij}(A,B) = -\int_A dt_1 \int_{B\cap[0,t_1]} dt_2 \,\mathrm{Im}[F_{im}(t_1)F_{jm}^*(t_2)]. \tag{S21}$$

The condition $W_{ip}\cap W_{jq} = \emptyset$ removes every equal-time target product but not the ordered products at $t_1 \neq t_2$. The exact rectangular-window evaluation, unequal-duration result, delay definitions, short-window conditions, and special cases are given in Section S2A.

The dedicated validation sets target leakage and dark-gap force to zero. It compares the analytic formula, direct complex time integration, and the complex Magnus recurrence for 1000 random parameter sets; the maximum absolute discrepancy is 4.44×10^{-15} rad. The calculation scans $\delta_m\Delta_c$, relative boundary phase, and signed mode coupling; the resulting data are used in Fig. 2 of the main text. Finally, local Z frames cannot reverse the interaction because they commute with $\sigma_i^z\sigma_j^z$.

S2.7 Idealized single-projector reduction and normalization

The 435 nm wavelength and the ${}^2S_{1/2} \leftrightarrow {}^2D_{3/2}$ level identity are taken from Ref. [1]. The reduction below adopts the ideal single-projector limit $P_1 = (\mathbb{I}+Z)/2$, and therefore $g_0 = g_z$; it is not a complete multilevel or device-calibrated derivation of the referenced apparatus. An apparatus-specific mapping requires user-supplied state-dependent couplings, detunings, polarization tensors, E2 matrix elements, beam geometry and power, linewidths, branching ratios, and measured or calculated scattering data.

Equation (S3) contains a single-state projector rather than a pure Pauli operator. Let

$$A_j(t) = \frac{\chi_j(t)}{2}, \qquad \Xi_j(t) = \Delta\boldsymbol{k}\cdot\boldsymbol{r}_j^0 - 2\pi\mu t - \phi_j(t). \tag{S22}$$

The zeroth- and first-order Lamb–Dicke terms are then

$$H_{\mathrm{Stark}}(t) = \hbar \sum_j A_j(t) \sin \Xi_j(t)[\mathbb{I} + \sigma_j^z], \tag{S23}$$

$$H_{\mathrm{force}}(t) = \hbar \sum_{j,m} A_j(t)\eta_{jm} \cos \Xi_j(t)[\mathbb{I} + \sigma_j^z] X_m(t), \tag{S24}$$

where $X_m(t) = a_m e^{-i\omega_m t} + a_m^\dagger e^{i\omega_m t}$. Thus the generalized coefficients are explicitly

$$g_{0,jm}(t) = g_{z,jm}(t) = \frac{\chi_j(t)}{2}\eta_{jm} c_j(t) = A_j(t)\eta_{jm} \cos \Xi_j(t), \qquad s_{0,j} = s_{z,j} = A_j \sin \Xi_j. \tag{S25}$$

The simulation coefficient called g_{jm} is $g_{z,jm}$. Using the nominal prefactor and scalar calibration defined in Eq. (S9),

$$g_{z,jm} = 2\pi f_{\mathrm{force}} \Omega_F^{(\mathrm{model})} f(t) s_j(t) \eta_{jm} c_j(t). \tag{S26}$$

Combining Eqs. (S25) and (S26) gives the complete projector inversion

$$\frac{\chi^{(\mathrm{map})}}{2\pi} = 2 f_{\mathrm{force}} \Omega_F^{(\mathrm{model})} = 2\Omega_F^{(\mathrm{eff})}, \qquad g_0 = g_z = \frac{\chi^{(\mathrm{map})}}{2}\eta c. \tag{S27}$$

The leading factor of 2 in Eq. (S27) follows from the projector decomposition, because $g_z/(2\pi\eta c)$ is one half of the differential projector light-shift amplitude $\chi/(2\pi)$. The symbolic target shift and any apparatus-specific power or scattering rescaling must therefore use this normalization. The simulated g_z, waveform calibration, pair phase, and differential displacement are evaluated directly from the reduced model.

The remaining normalization factors are independent. The effective input $\Omega_F^{(\mathrm{eff})}$ is converted from hertz to angular frequency once through 2π; η_{jm} is then applied once in Eq. (S26). Writing $c_j = \cos\theta_j = (e^{i\theta_j} + e^{-i\theta_j})/2$ assigns one half to each positive/negative-frequency quadrature, but their sum reconstructs the real-force coefficient and introduces no additional net factor. For the adopted two-field equal-amplitude convention, the traveling projector shift is written symbolically as $\chi = \Omega_A\Omega_B/(2\Delta)$, which reduces to $2\Omega^2/(4\Delta)$ for $\Omega_A = \Omega_B = \Omega$. This is a normalization convention in the idealized reduction, not a device-calibrated coupling model or a sum over an arbitrary beam multiplicity.

Three different objects must not be conflated. Here $\mathbb{I}$ denotes the global identity on the spin register. The term $s_{0,j}\mathbb{I}$ is a motion-independent scalar energy shift and contributes only a common dynamical phase. The term $g_{0,jm}\mathbb{I}X_m$ is a spin-independent *motional force*; it displaces the oscillator and cannot be discarded as a global scalar phase. The term $g_{z,jm}\sigma_j^z X_m$ is the spin-dependent force that produces branch-dependent displacement and pairwise ZZ phase.

Define $G_{0m}(t) = \sum_j g_{0,jm}(t)$ and

$$B_m(t) = G_{0m}(t)\mathbb{I} + \sum_j g_{z,jm}(t)\sigma_j^z. \tag{S28}$$

The first Magnus term can be written

$$\begin{aligned} \Omega_1 = {} & \sum_m (\beta_m a_m^\dagger - \beta_m^* a_m)\mathbb{I} + \sum_{j,m} (\alpha_{jm} a_m^\dagger - \alpha_{jm}^* a_m)\sigma_j^z \\ & - i\zeta_0 \mathbb{I} - i \sum_j \zeta_j \sigma_j^z, \end{aligned} \tag{S29}$$

with

$$\beta_m = -i \int_0^T G_{0m}(t) e^{i\omega_m t} dt, \quad \alpha_{jm} = -i \int_0^T g_{z,jm}(t) e^{i\omega_m t} dt, \tag{S30}$$

and $\zeta_0 = \int_0^T \sum_j s_{0,j} dt$, $\zeta_j = \int_0^T s_{z,j} dt$. The common displacement β_m moves every spin branch together, whereas α_{jm} controls the branch separation and spin–motion coherence.

Because all $\mathbb{I}$ and Z spin operators commute, the force part of the second Magnus term is

$$\Omega_2 = i \sum_m \int_0^T dt_1 \int_0^{t_1} dt_2 \, \sin[\omega_m(t_1 - t_2)] B_m(t_1) B_m(t_2). \tag{S31}$$

Expanding $B_m(t_1)B_m(t_2)$ gives four classes:

$$\gamma = \sum_m \iint_{t_2<t_1} \sin[\omega_m(t_1 - t_2)] \left[G_{0m}(t_1)G_{0m}(t_2) + \sum_j g_{z,jm}(t_1) g_{z,jm}(t_2) \right] dt_2 dt_1, \tag{S32}$$

$$\lambda_j^{(\mathrm{geom})} = \sum_m \iint_{t_2<t_1} \sin[\omega_m(t_1 - t_2)] \left[G_{0m}(t_1) g_{z,jm}(t_2) + g_{z,jm}(t_1) G_{0m}(t_2) \right] dt_2 dt_1, \tag{S33}$$

$$\Phi_{ij} = \sum_m \iint_{t_2<t_1} \sin[\omega_m(t_1 - t_2)] \left[g_{z,im}(t_1) g_{z,jm}(t_2) + g_{z,jm}(t_1) g_{z,im}(t_2) \right] dt_2 dt_1. \tag{S34}$$

Here γ is a global geometric phase, $\lambda_j = \lambda_j^{(\mathrm{geom})} - \zeta_j$ is the total local-Z phase in the exponent, and Φ_{ij} is the pairwise ZZ phase. The identity–Z cross term therefore produces local Z, not an additional ZZ coupling.

These expressions prove the reduction boundary. At fixed g_z, g_0 does not change Φ_{ij}, α_{jm}, or the spectator-ZZ matrix. It does change absolute motional closure through β_m and generally creates deterministic local phases through $\lambda_j^{(\mathrm{geom})}$. A virtual-$Z$ update can remove a known λ_j, but cannot remove β_m, residual α_{jm}, or Φ_{ij}. A spin echo flips Z while leaving the identity force unchanged; under a symmetric toggling schedule it can cancel odd-in-Z Stark and identity–Z terms while retaining an even ZZ term, but it does not by itself close the common displacement. Physical cancellation of g_0 requires a balanced force, for example equal-and-opposite forces on the two qubit states. The balanced model used here is an ideal symmetry benchmark and is not an assertion that the 435 nm architecture implements that additional control.

Sections 2.1 and 2.5 of the main text define the pure-Z, idealized single-projector, and ideal balanced force structures; Section 3.2 compares their aggregate coordinates, and Fig. 3 shows the optimized idealized single-projector waveform and reduced-channel diagnostics. This subsection provides the corresponding normalization and Magnus derivation. At fixed g_z, the pure-Z and idealized single-projector calculations agree in α_{jm}, Φ_{ij}, and the spectator-ZZ matrix, while the idealized single-projector calculation additionally includes β_m and the identity–Z contribution to λ_j. The ideal balanced model is a separate symmetry benchmark with $g_0 = 0$. Figure S1 gives the mode-resolved decomposition.

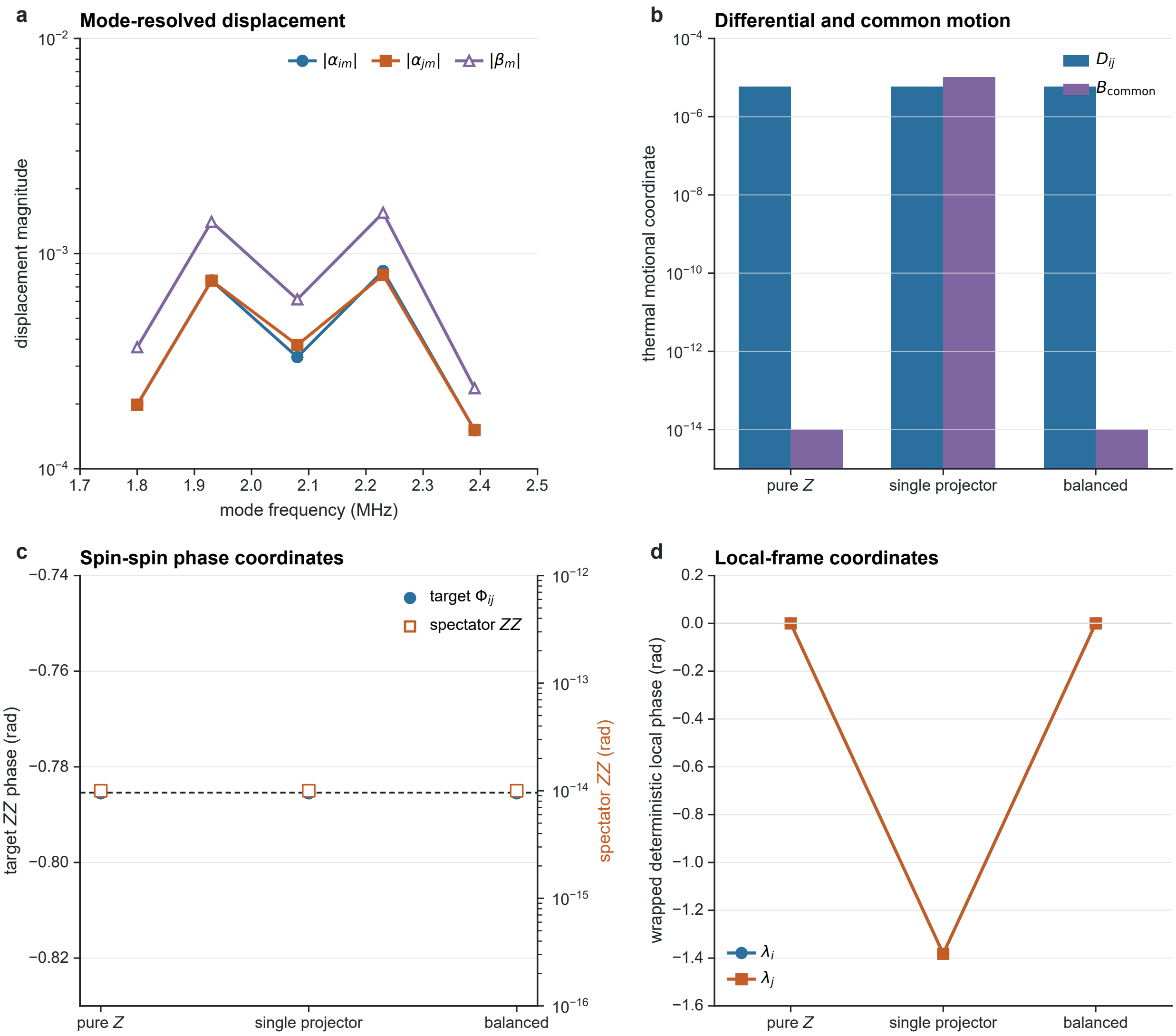

Supplementary Figure S1: Mode-resolved common and differential motion in the idealized single-projector limit. The panels give the mode-resolved idealized single-projector decomposition corresponding to the model coordinates discussed in Sections 2.5 and 3.2 of the main text: the common displacement β_m, target differential displacements α_{im} and α_{jm}, pairwise ZZ phase, and deterministic local-Z phases before virtual-frame correction.

S2.8 Notation and unit conventions

Supplementary Table S1: Notation and unit conventions. Stored units refer to the configuration and CSV interfaces; equations use SI time and radians unless stated otherwise.

Symbol or field	Meaning	Stored/reported unit	Conversion used in equations
t, T, g, σ_t	time, duration, dark gap, timing jitter	microseconds in input tables; seconds internally	multiply microseconds by 10^{-6}
$\Omega_F^{(\mathrm{model})}$, f_{force}, $\Omega_F^{(\mathrm{eff})}$	nominal cyclic-frequency prefactor, dimensionless scalar calibration, and effective prefactor	Hz, dimensionless, Hz	$\Omega_F^{(\mathrm{eff})} = f_{\mathrm{force}}\Omega_F^{(\mathrm{model})}$; $g_z = 2\pi\Omega_F^{(\mathrm{eff})}\eta c$; $\chi^{(\mathrm{map})}/(2\pi) = 2\Omega_F^{(\mathrm{eff})}$
$\Omega_{q\ell b}$	state-resolved atomic-transition coupling	rad s^{-1}	used only when transition-resolved apparatus inputs are supplied; no additional 2π
ν_m	ordinary motional-mode frequency	Hz internally; MHz in tables	$\omega_m = 2\pi\nu_m$
ω_m	angular motional frequency	rad s^{-1}	used in $e^{\pm i\omega_m t}$
μ	programmed force-quadrature frequency	Hz	phase rate $2\pi\mu$
Δf_{AOD}, Δf_{AOM}, δ_{res}	steering shift, compensation, residual offset	Hz	enter $2\pi\int\delta_j\,dt$
δ_j	residual beat-note detuning after compensation	Hz	$\delta_j = \Delta f_{\mathrm{AOD}} - \Delta f_{\mathrm{AOM}} + \delta_{\mathrm{res}}$
δ_{jm}	near-sideband angular detuning	rad s^{-1}	$2\pi(\mu + \delta_j - \nu_m)$
θ_j, ϕ_+, ϕ_-	force-quadrature and positive/negative-frequency offsets	radians	added only as dimensionless phases
$\phi_{\mathrm{DDS}}, \phi_{\mathrm{AOD}}, \phi_{\mathrm{opt}}$	programmed and relative optical-path offsets	radians	added only as dimensionless phases
η_{jm}	signed Lamb–Dicke participation	dimensionless	no unit conversion
$g_{jm}^{(\mathrm{real})}$	full real-force reference coefficient	rad s^{-1}	Eq. (S11); retains both frequency quadratures
F_{jm}	complex near-resonant force coefficient	rad s^{-1}	Eq. (S13); includes detuning and boundary phase once
$g_{0,jm}$, $g_{z,jm}$	identity and differential motional-force coefficients	rad s^{-1}	$g_{0,jm} = g_{z,jm}$; the simulated coefficient is $g_{jm} \equiv g_{z,jm}$ in the idealized single-projector limit
$s_{0,j}$, $s_{z,j}$	common and differential motion-independent Stark coefficients	rad s^{-1}	integrated directly to global/local phases
β_m	common identity-force displacement	dimensionless complex amplitude	time integral of $G_{0m} = \sum_j g_{0,jm}$
α_{jm}	residual displacement amplitude	dimensionless complex amplitude	$-i\int F_{jm}^* dt$ in the analytic RWA; full-real reference uses $-i\int g_{jm}^{(\mathrm{real})} e^{i\omega_m t} dt$
λ_j	total deterministic local-Z phase	radians	identity–Z geometric term minus integrated $s_{z,j}$
Φ_{ij}	accumulated pair phase	radians	ordered second-order integral
Γ_{sc}, $\dot{\bar{n}}_m$	scattering and heating rates	s^{-1}	reported as $\Gamma_{\mathrm{sc}}T$ and $\dot{\bar{n}}_m T$

S2A. Disjoint-Window Symplectic-Phase Identity

For a force window W_{jp}, use the complex near-resonant Hamiltonian

$$H_I^{(\mathrm{RWA})}(t) = \hbar \sum_{j,m} \sigma_j^z \left[F_{jm}(t) a_m + F_{jm}^*(t) a_m^\dagger\right] \tag{S35}$$

and define the mode-resolved displacement increment

$$\delta\alpha_{jm}^{(p)} = -i \int_{W_{jp}} dt\, F_{jm}^*(t). \tag{S36}$$

This is the first-Magnus displacement generated by that window before summing over all windows on the same ion. If a constant programmable boundary phase shifts the force as $F_{jm} \to F_{jm} e^{i\phi_{jp}}$, the increment rotates as

$$\delta\alpha_{jm}^{(p)} \to \delta\alpha_{jm}^{(p)} e^{-i\phi_{jp}}. \tag{S37}$$

A phase varying within a window remains inside Eq. (S36) and is not a rigid rotation.

S2A.1 Two-window formula and time ordering

Consider two disjoint windows, W_{ip} and W_{jq}, on different ions and the same mode. If W_{ip} occurs before W_{jq}, the contribution to the ZZ phase is the oriented phase-space area

$$\Phi_{ij,m}^{(p\prec q)} = \mathrm{Im}\Big[\delta\alpha_{jm}^{(q)} \left(\delta\alpha_{im}^{(p)}\right)^*\Big]. \tag{S38}$$

If the time order is reversed, the sign is reversed for the same two displacement vectors:

$$\Phi_{ij,m}^{(q\prec p)} = \mathrm{Im}\Big[\delta\alpha_{im}^{(p)} \left(\delta\alpha_{jm}^{(q)}\right)^*\Big] = -\,\mathrm{Im}\Big[\delta\alpha_{jm}^{(q)} \left(\delta\alpha_{im}^{(p)}\right)^*\Big]. \tag{S39}$$

Equivalently, the bosonic displacement product $D(\delta\alpha_b)D(\delta\alpha_a)$ accumulates the Weyl phase $\mathrm{Im}(\delta\alpha_b\delta\alpha_a^*)$, so reversing the ordering reverses the oriented area.

Let the first window start at t_i and last τ_i. Let the second start at $t_j > t_i + \tau_i$ and last τ_j. Define the dark gap, start-to-start delay, window centers, and center-to-center delay as

$$g = t_j - (t_i + \tau_i), \qquad \Delta_s = t_j - t_i = \tau_i + g, \tag{S40}$$

$$c_i = t_i + \frac{\tau_i}{2}, \qquad c_j = t_j + \frac{\tau_j}{2}, \qquad \Delta_c = c_j - c_i = \Delta_s + \frac{\tau_j - \tau_i}{2}. \tag{S41}$$

Within each rectangular window write

$$F_{qm}(t) = A_q e^{i(\delta_{qm}t+\phi_q)}, \qquad \delta_{qm} = 2\pi(\mu + \delta_q - \nu_m), \tag{S42}$$

where A_q is a real signed near-resonant amplitude in rad s^{-1} and $\Delta\phi = \phi_j - \phi_i$. Direct integration gives

$$\delta\alpha_{qm} = -iA_q\tau_q\,\mathrm{sinc}\!\left(\frac{\delta_{qm}\tau_q}{2}\right) e^{-i(\delta_{qm}c_q+\phi_q)}, \qquad \mathrm{sinc}\,x = \frac{\sin x}{x}. \tag{S43}$$

Therefore the unequal-duration, unequal-detuning result is

$$\begin{aligned}\Phi_{ij,m}^{(i\prec j)} &= A_iA_j\tau_i\tau_j\,\mathrm{sinc}\!\left(\frac{\delta_{im}\tau_i}{2}\right)\mathrm{sinc}\!\left(\frac{\delta_{jm}\tau_j}{2}\right)\\ &\quad\times \sin(\delta_{im}c_i - \delta_{jm}c_j + \phi_i - \phi_j).\end{aligned} \tag{S44}$$

For a common compensated drive, $\delta_{im} = \delta_{jm} = \delta_m$, this reduces to

$$\Phi_{ij,m}^{(i\prec j)} = -A_iA_j\tau_i\tau_j\,\mathrm{sinc}\!\left(\frac{\delta_m\tau_i}{2}\right)\mathrm{sinc}\!\left(\frac{\delta_m\tau_j}{2}\right)\sin(\delta_m\Delta_c + \Delta\phi). \tag{S45}$$

For equal durations, $\Delta_c = \Delta_s = \tau + g$. The laboratory mode frequency ω_m and drive frequency $2\pi(\mu + \delta_j)$ occur only through their difference δ_{jm} after the RWA; the discarded full-real-force quadrature instead oscillates at their sum.

If $|\delta_{im}|\tau_i/2 \ll 1$ and $|\delta_{jm}|\tau_j/2 \ll 1$, the exact center-time phase is preserved while the sinc factors approach unity:

$$\Phi_{ij,m}^{(p\prec q)} \simeq A_iA_j\tau_i\tau_j \sin(\delta_{im}c_i - \delta_{jm}c_j + \phi_i - \phi_j). \tag{S46}$$

For the equal-duration scan used in Fig. 2 of the main text, the finite-window amplitude correction is reported as

$$\epsilon_K = \left|1 - \mathrm{sinc}^2\!\left(\frac{\delta_m\tau}{2}\right)\right|. \tag{S47}$$

This compares the exact finite-window amplitude factor with the nonzero short-window reference τ^2 and is independent of zeros of the sinusoidal phase factor. A secondary source-data diagnostic uses the denominator $\max(|K_{\mathrm{exact}}|, 10^{-30}\,\mathrm{s}^2)$. The floor regularizes numerical storage, but the diagnostic remains singular as $K_{\mathrm{exact}} \to 0$ and is therefore excluded from the main figures. Replacing Δ_c by Δ_s for unequal durations requires the additional condition $|\delta_m||\tau_j - \tau_i|/2 \ll 1$. The phase vanishes as either duration tends to zero. A π shift of one boundary phase or reversal of one signed Lamb–Dicke factor flips the sign. At zero detuning it becomes $-A_iA_j\tau_i\tau_j\sin\Delta\phi$; it vanishes for equal boundary quadratures. A nonzero integer cycle $\delta_m\tau_q = 2\pi n$ cancels the corresponding window increment through the sinc factor.

S2A.2 Multi-window and multi-mode formula

Let $a \prec b$ denote that window a ends before window b begins. The second-Magnus coefficient of a fixed Z_iZ_j operator is

$$\Phi_{ij} = -\sum_m \int_0^T dt_1 \int_0^{t_1} dt_2 \; \mathrm{Im}\big[F_{im}(t_1)F_{jm}^*(t_2) + F_{jm}(t_1)F_{im}^*(t_2)\big] . \tag{S48}$$

Writing $F_{im} = \sum_p F_{im}^{(p)}$ and $F_{jm} = \sum_q F_{jm}^{(q)}$, each disjoint target-window pair has exactly one order: $W_{ip} \prec W_{jq}$ or $W_{jq} \prec W_{ip}$. The two ordered terms in Eq. (S48) therefore reduce to one oriented area for each target-window pair. For a fixed ion pair (i, j),

$$\Phi_{ij} = \sum_m \sum_{\substack{a\prec b \\ \{\ell(a),\ell(b)\}=\{i,j\}}} \mathrm{Im}\left[\delta\alpha_{\ell(b)m}^{(b)} \left(\delta\alpha_{\ell(a)m}^{(a)}\right)^*\right], \tag{S49}$$

where $\ell(a)$ is the ion addressed in window a. The set equality is essential: it excludes same-ion areas and all windows involving spectator ions. Those terms contribute to other pair phases, single-channel geometric phases, or spectator couplings, but not to the fixed coefficient Φ_{ij}. This is identical to the ordered complex-force integral because

$$\mathrm{Im}\left[\delta\alpha_{\ell(b)m}^{(b)} \left(\delta\alpha_{\ell(a)m}^{(a)}\right)^*\right] = -\int_{W_b} dt_1 \int_{W_a} dt_2 \; \mathrm{Im}\left[F_{\ell(b)m}(t_1)F_{\ell(a)m}^*(t_2)\right] . \tag{S50}$$

S2A.3 Exact identity and sufficient dominance conditions

Proposition 1 states an identity, not an independent interaction mechanism. Disjoint target supports remove equal-time products, but every temporally ordered pair of target windows contributes the symplectic product in Eq. (S49). Define the exact mode-resolved group

$$\Phi_{ij}^{(m)} = \sum_{\substack{a\prec b \\ \{\ell(a),\ell(b)\}=\{i,j\}}} \mathrm{Im}\left[\delta\alpha_{\ell(b)m}^{(b)} \left(\delta\alpha_{\ell(a)m}^{(a)}\right)^*\right] . \tag{S51}$$

If a mode m_0 obeys

$$\left|\Phi_{ij}^{(m_0)}\right| > \sum_{m\neq m_0} \left|\Phi_{ij}^{(m)}\right|, \tag{S52}$$

then the reverse triangle inequality gives

$$|\Phi_{ij}| \geq \left|\Phi_{ij}^{(m_0)}\right| - \sum_{m\neq m_0} \left|\Phi_{ij}^{(m)}\right| > 0. \tag{S53}$$

The remainder cannot cross zero, so $\operatorname{sgn}\Phi_{ij} = \operatorname{sgn}\Phi_{ij}^{(m_0)}$.

An analogous exact grouping is available at the ordered-window-pair level. Let

$$K_{ab}^{ij} = \sum_m \mathrm{Im}\left[\delta\alpha_{\ell(b)m}^{(b)} \left(\delta\alpha_{\ell(a)m}^{(a)}\right)^*\right], \qquad a \prec b, \quad \{\ell(a),\ell(b)\} = \{i,j\}. \tag{S54}$$

If one pair (a_0, b_0) satisfies

$$\left|K_{a_0b_0}^{ij}\right| > \sum_{(a,b)\neq(a_0,b_0)} \left|K_{ab}^{ij}\right|, \tag{S55}$$

then the total phase is nonzero and has the sign of $K_{a_0b_0}^{ij}$. Both inequalities are sufficient but not necessary. Their failure means only that the exact contributions require explicit summation.

For comparison with the exact groups, a multi-window heuristic motivated by the short-window approximation in the main text replaces each finite-window increment by

$$\widetilde{\delta\alpha}_{\ell(a)m}^{(a)} = -i\exp\big[-i\arg F_{\ell(a)m}(c_a)\big] \int_{W_a} dt \; \big|F_{\ell(a)m}(t)\big| , \tag{S56}$$

where c_a is the amplitude-weighted window center, and inserts these approximate vectors into Eq. (S49). This construction omits phase evolution within a finite window. It is therefore a diagnostic S_{ij}^{heur}, not an exact nonzero-phase or sign criterion.

The single-mode limit is obtained by dropping the sum over m. Complete cancellation occurs when the sum of all oriented areas in Eq. (S49) vanishes, even if individual window-pair areas are nonzero. A sign reversal occurs if the net oriented area changes sign, for example by reversing the ordering of otherwise fixed increments, changing the sign of a signed Lamb–Dicke product or force amplitude, or rotating one boundary phase by approximately π.

S2A.4 Geometric interpretation of phase-clock rules

The continuous rule preserves the laboratory-time phase of successive displacement increments, so the oriented areas can add coherently. The reset rule reinitializes each local quadrature and therefore rotates subsequent $\delta\alpha$ vectors relative to the accumulated phase-space polygon. The scrambled rule assigns independent boundary rotations; its ensemble-averaged oriented area is suppressed even though individual runs may have nonzero areas. The gap-frozen rule keeps the force envelope fixed but removes the phase advance accumulated through dark gaps, rotating later increments by a deterministic counterfactual angle.

S2A.5 Numerical identity check

The validation data contain 1000 random full-real-force identity schedules and 1000 random rectangular complex-RWA parameter sets. For the latter, the laboratory mode frequency, drive frequency, detuning, durations, dark gap, start and center delays, signed amplitudes, and relative boundary phase are sampled independently within the specified ranges. The analytic finite-window expression, direct complex Gauss integration, and complex Magnus recurrence agree with maximum absolute discrepancy 4.44×10^{-15} rad and maximum relative discrepancy 6.20×10^{-12} for nonzero cases above the 10^{-12}-rad denominator floor. The numerical checks also cover the zero-duration limit, a π boundary shift, reversal of fixed displacement-vector order, zero detuning, integer-cycle cancellation, unequal durations, and signed-mode reversal.

Supplementary Table S2: Deterministic symplectic sign controls.

Control	reference (rad)	transformed (rad)	sign residual (rad)
window-order reversal	0.0204000	-0.0204000	1.15×10^{-15}
boundary-phase π shift	0.0204000	-0.0204000	0
signed mode-coupling reversal	0.0204000	-0.0204000	0

The maximum deterministic sign-control discrepancy is 1.15×10^{-15} rad, below the numerical acceptance threshold of 10^{-9} rad, confirming the discrete-grid symplectic identity for the implemented reduced Hamiltonian.

S2A.6 Representative-chain sign analysis

The comparison uses near, middle, and far target pairs in physical 5-, 10-, 20-, and 30-ion normal-mode chains. Each pair uses the boundary offset and force scale selected by the fixed-schedule atlas, while scalar leakage and dark-gap force are set to zero. The exact complex-RWA Magnus phase and the sum of all ordered window products agree to a maximum absolute residual of 1.78×10^{-14} rad. The mode-dominance condition certifies 6 of 12 points (50.0%), while the window-pair condition certifies 0 of 12 points. The short-window heuristic has one sign mismatch (8.3%).

Supplementary Table S3: Sufficient-condition and heuristic-sign comparison for representative physical-chain pairs. Ion indices are one-based. "Mode" and "window pair" report whether the corresponding strict triangle inequality is satisfied; "heuristic match" compares sgn S_{ij}^{heur} with the exact symplectic phase. Failure of a sufficient condition is not a phase-cancellation result.

N	pair	mode	window pair	heuristic match
5	near (1–2)	yes	no	yes
5	middle (2–4)	yes	no	yes
5	far (1–5)	no	no	yes
10	near (1–2)	no	no	yes
10	middle (5–7)	no	no	yes
10	far (1–10)	yes	no	yes
20	near (1–2)	no	no	yes
20	middle (10–12)	yes	no	yes
20	far (1–20)	yes	no	yes
30	near (1–2)	no	no	yes
30	middle (15–17)	yes	no	no
30	far (1–30)	no	no	yes

The authors' working reproducibility tree records the full mode contributions, ordered-window-pair contributions, triangle margins, and heuristic errors under the internal filename `data/dominant_mode_sufficient_condition.csv`. Source data and code are available from the corresponding authors upon reasonable request, as stated in Section S18.

S3. Baseline Parameters and Hardware Inputs

Supplementary Table S4: Baseline chain, force, and timing parameters.

Quantity	Value	Interpretation boundary
Ion species and baseline chain	$^{171}\mathrm{Yb}^{+}$, 5 ions	Representative chain for mechanism tests
Optical platform identity	435 nm, $^{2}S_{1/2} \leftrightarrow {}^{2}D_{3/2}$ E2 transition	Wavelength and levels verified from Ref. [1]; trap geometry remains illustrative
Target pair	ions 2 and 4 in one-based chain labelling	Selected two-ion operation embedded in a chain
Radial mode frequencies	1.800, 1.930, 2.080, 2.230, 2.390 MHz	Representative spectrum, not measured normal modes
Thermal occupations $\bar{n}_m$	0.8, 0.7, 0.5, 0.4, 0.3	Used only for residual-displacement weighting
Nominal model force-frequency prefactor $\Omega_F^{(\mathrm{model})}$	75 kHz before scalar force calibration	Reduced-force-model input; calibrated schedules report the dimensionless multiplier f_{force}
Two-beam force beat note	1.816 MHz	Representative detuned-force frequency
Target ZZ phase	$-\pi/4$	Signed simulation target; circuit use needs local frames
Control schedule	12 cycles; 8.0 microsecond windows; 2.0 microsecond gaps	Alternating non-overlapping target windows
Rise/fall and time step	0.4 microsecond; 0.08 microsecond	Smooth envelope and numerical integration grid
Total sequence time	240 microseconds	Baseline representative duration

Supplementary Table S5: Baseline signed Lamb–Dicke matrix and optical phase offsets. Ion labels are one-based. The illustrative matrix uses the wave-vector magnitude associated with the 435 nm wavelength identified in Ref. [1]; it is not a measured apparatus matrix.

Ion	$\eta_{1.800}$	$\eta_{1.930}$	$\eta_{2.080}$	$\eta_{2.230}$	$\eta_{2.390}$	$\phi_{\rm opt}$ (rad)
1	0.03874	0.01890	0.00945	0.00567	0.00378	0.00
2	0.04063	0.01134	-0.01134	-0.00567	0.00283	0.37
3	0.04157	-0.01323	0.00000	0.00661	-0.00378	0.71
4	0.04063	0.01134	0.01134	-0.00567	-0.00283	1.05
5	0.03874	-0.01890	-0.00945	0.00567	0.00378	1.39

Supplementary Table S6: AOD/AOM, noise, and numerical scan inputs.

Quantity	Value	Role in the present model
AOD frequency shifts	$-40, -20, 0, 20, 40$ kHz	Ion-channel frequency offsets
AOM compensation values	$-40, -20, 0, 20, 40$ kHz	Nominal cancellation of AOD shifts
Global residual detuning	0 Hz baseline; scan from -5 to 5 kHz	Calibration sensitivity axis
Addressing leakage	0.006 baseline; scan to 0.05	Spectator-force stress test
Window phase noise	0.015 rad baseline; scan to 0.1 rad	Phase-clock coherence robustness axis
Intensity noise	0.006 fractional rms	Representative light-shift amplitude input
Heating input	30 quanta/s	Order-of-magnitude displacement-weight input
Scattering input	3 s^{-1}	Order-of-magnitude input, not a multilevel calculation
Baseline phase-rule replicates	120 stochastic replicates	Mechanism-level phase-control scan; the hardware-robustness grids in Section S17 use 512 realizations per point

The baseline leakage value is included to keep target-versus-spectator diagnostics visible in representative scans. The existence of the selected-pair phase is tested separately in the zero-leakage limit, where the targets never share an active force window and the validation suite still obtains the calibrated nonzero cross-time ZZ phase.

The AOM row is listed in the same sign convention used by the phase accumulator. The residual ion-dependent detuning is

$$\delta_j = \delta_j^{\rm AOD} - \delta_j^{\rm AOM} + \delta_{\rm global}.$$

Thus equal listed AOD and AOM values correspond to cancellation in the baseline configuration.

Scattering and heating are bookkeeping coordinates only:

$$p_{\rm sc} = \Gamma_{\rm sc} T_{\rm seq}, \qquad \Delta\bar{n} = \dot{\bar{n}} T_{\rm seq}. \tag{S57}$$

At the illustrative inputs $\Gamma_{\rm sc} = 3\ \mathrm{s}^{-1}$, $\dot{\bar{n}} = 30\ \mathrm{s}^{-1}$, and $T_{\rm seq} = 240\ \mu\mathrm{s}$, these coordinates are 7.2×10^{-4} and 7.2×10^{-3}. Device-level values require measured mode-resolved heating and complete or measured scattering data.

When transition-resolved inputs are supplied, the apparatus interface evaluates the weak-excitation estimates

$$\delta\omega_q \simeq \sum_{\ell,b} \frac{|\Omega_{q\ell b}|^2}{4\Delta_{q\ell}}, \qquad \Gamma_{{\rm sc},q} \simeq \sum_{\ell,b} \frac{\Gamma_{q\ell}|\Omega_{q\ell b}|^2}{4\Delta_{q\ell}^2}. \tag{S58}$$

For the E2 example, $\Omega_{q\ell}$ must come from a user-supplied effective Rabi coefficient or field-gradient calculation; the reduced force scale is not substituted for an atomic coupling. The projector normalization is

$$\Delta^{\rm (map)}_{\rm LS,target}/(2\pi) = 2 f_{\rm force} \Omega_F^{\rm (model)} = 2\Omega_F^{\rm (eff)}, \tag{S59}$$

where the factor 2 inverts the 1/2 in $P_1 = (\mathbb{I} + Z)/2$. This relation maps control normalization only and does not determine optical power.

Supplementary Table S7: Inputs required for apparatus-specific transfer. Missing atomic or apparatus inputs disable the corresponding prediction rather than being inferred from the reduced force scale.

Input	Use in the model	Status when absent
Detunings, linewidths, branching ratios, and polarization factors	Differential light shift and scattering sums	Atomic-data calculation disabled
E2 coupling or field-gradient coefficient	Converts intensity to the state-resolved Rabi rate	Power and scattering fields left blank
Beam waist, power, and beam count	Converts optical geometry to intensity	No optical-power estimate
AOD switching phase and dark-gap extinction	Enters the boundary phase and residual-force stress models	Reported only as scan coordinates
Pair-resolved leakage and mode drift/heating	Replaces scalar leakage and representative motional inputs	Device-specific spectator and motional responses not evaluated without these inputs
Common/differential force and Stark couplings	Determines β_m, α_{jm}, and λ_j in the projector model	Projector-specific fields left blank
Measured scattering rate or upper bound	External comparison coordinate	Used only for comparison with the model output

The machine-readable interface distinguishes bookkeeping estimates, calculations based on user-supplied atomic data, and measured comparison inputs. Optical-power and scattering estimates are left undefined when the required inputs are unavailable.

S4. Conditional-Ramsey Protocol and Reduced-Channel Validation

S4.1 Protocol and matched-envelope controls

This section derives the observable from the conditional motional trajectories. The exact branch contrast is denoted by C_z, whereas e^{-D} is used only as a two-target closure proxy. The protocol uses a matched-envelope search whose objective and selection coordinates are the exact thermal contrast, the Weyl-overlap phase, and phase separation modulo $\pi/2$. The search spans window duration, dark gap, cycle count, target mode, beat-note detuning, cycle-amplitude modulation, relative boundary phase, bounded phase increments, and continuous-rule force calibration. The selected envelope uses 10 cycles, 10.000 μs windows, 2.000 μs gaps, a beat note 16.000 kHz above the lowest representative mode, and force scale 2.988438. The same envelope, timing, and force scale are then used for continuous, reset, scrambled, and gap-frozen-equivalent rules. A separately optimized continuous-rule envelope was evaluated in the authors' working data as a contrast-loss control and is not used to assess measurable phase redirection. All traces and channel metrics are model-level estimates for a proposed test, not experimental state characterization.

Both ions are first prepared in

$$|++\rangle = \frac{1}{2}(|0\rangle + |1\rangle)_i(|0\rangle + |1\rangle)_j. \tag{S60}$$

With $Z|0\rangle = -|0\rangle$ and $Z|1\rangle = +|1\rangle$, apply H_j followed by no operation or by X_j to obtain $|+\rangle_i|z\rangle_j$, where $z = -1$ or $+1$. Every spectator ion is prepared in a known Z eigenstate and held fixed across the two branch measurements; the representative protocol does not include spectators in superposition. Each known branch receives the same sequential interaction

$$U_{ZZ} = \exp(i\Phi_{ij}Z_iZ_j). \tag{S61}$$

The experimentally calibrated propagator can also contain commuting local terms,

$$U_{\mathrm{seq}} = e^{i\lambda_0}e^{i\lambda_iZ_i+i\lambda_jZ_j}U_{ZZ}. \tag{S62}$$

Virtual updates $F = R_z^{(i)}(2\lambda_i)R_z^{(j)}(2\lambda_j)$ cancel these terms for $R_z(\vartheta) = e^{-i\vartheta Z/2}$. They cannot flip the ZZ branch, remove motional overlap phases, or replace the two-branch subtraction. The symbol β_m is reserved for the common motional displacement and is not used for local phases.

S4.2 Exact conditional-displacement contrast for the two-branch Ramsey protocol

For a diagonal spin-dependent force, the propagator after the force sequence can be resolved in the computational basis as

$$U(T) = \sum_{\boldsymbol{z}} |\boldsymbol{z}\rangle\langle\boldsymbol{z}|\, D[\boldsymbol{A}(\boldsymbol{z})]e^{i\Theta(\boldsymbol{z})}, \qquad A_m(\boldsymbol{z}) = \beta_m + \sum_k z_k\alpha_{km}, \tag{S63}$$

where $z_k = \pm 1$, $D(\boldsymbol{A}) = \prod_m D_m(A_m)$, β_m is the identity-force displacement, and α_{km} is the local Z_k-force displacement. The spin phase is

$$\Theta(\boldsymbol{z}) = \gamma + \sum_k \lambda_k z_k + \sum_{k<l} \Phi_{kl} z_k z_l. \tag{S64}$$

In the conditional-Ramsey protocol, ion j is prepared in the known branch $z_j = z$ and ion i forms the two arms $z_i = -1$ (arm 0) and $z_i = +1$ (arm 1). Fixed spectator branches are collected in

$$A_{\mathrm{spec},m} = \sum_{k\neq i,j} z_k\alpha_{km}. \tag{S65}$$

The two final displacements are therefore

$$A_{0,z,m} = \underbrace{\beta_m}_{\text{identity force}} \quad \underbrace{-\alpha_{im} + z\alpha_{jm} + A_{\mathrm{spec},m}}_{\text{local forces}}, \tag{S66}$$

$$A_{1,z,m} = \underbrace{\beta_m}_{\text{identity force}} \quad \underbrace{+\alpha_{im} + z\alpha_{jm} + A_{\mathrm{spec},m}}_{\text{local forces}}. \tag{S67}$$

Consequently,

$$\Delta\alpha_{z,m} = A_{1,z,m} - A_{0,z,m} = 2\alpha_{im}. \tag{S68}$$

The common identity displacement, the known ion-j branch, and every fixed spectator branch cancel from the arm difference. They need not vanish individually.

For an initially factorized thermal motional state

$$\rho_{\mathrm{th}} = \bigotimes_m \rho_{\mathrm{th},m}, \qquad \rho_{\mathrm{th},m} = \sum_{n=0}^{\infty} \frac{\bar{n}_m^n}{(1+\bar{n}_m)^{n+1}} |n\rangle\langle n|, \tag{S69}$$

the ion-i Ramsey coherence contains

$$\mathcal{L}_z = \mathrm{Tr}_{\mathrm{mot}}\Big[D(\boldsymbol{A}_{0,z})\rho_{\mathrm{th}} D^\dagger(\boldsymbol{A}_{1,z})\Big] \tag{S70}$$

$$= \exp\big[i\vartheta_z^{\mathrm{mot}}\big] \exp\left[-\frac{1}{2}\sum_m (2\bar{n}_m+1)|\Delta\alpha_{z,m}|^2\right], \tag{S71}$$

where the Weyl-overlap phase is

$$\vartheta_z^{\mathrm{mot}} = \mathrm{Im}\sum_m A^*_{1,z,m}A_{0,z,m}. \tag{S72}$$

Thus the exact branch contrast is

$$C_z = |\mathcal{L}_z| = \exp\left[-\frac{1}{2}\sum_m (2\bar{n}_m+1)|\Delta\alpha_{z,m}|^2\right] = \exp\left[-2\sum_m (2\bar{n}_m+1)|\alpha_{im}|^2\right]. \tag{S73}$$

For the specified diagonal force and known-branch protocol, $C_+ = C_-$ even though the overlap phases can differ.

After deterministic local-Z frame correction, the exact branch-corrected fringe is

$$\widetilde{\Pi}_z(\varphi) = -C_z \sin\bigl[\varphi + 2z\Phi_{ij} - \vartheta_z^{\mathrm{mot}}\bigr]. \tag{S74}$$

The motional-overlap phase must therefore be included when interpreting a nonclosed trajectory. It is not a contrast loss and is not removed by replacing C_z with an empirical factor.

For a general initial spin density matrix, no single visibility factor is sufficient. The exact reduced spin element is

$$\rho_{\boldsymbol{z},\boldsymbol{z}'}(T) = \rho_{\boldsymbol{z},\boldsymbol{z}'}(0) e^{i[\Theta(\boldsymbol{z})-\Theta(\boldsymbol{z}')]} e^{i\,\mathrm{Im}\sum_m A_m(\boldsymbol{z}')^* A_m(\boldsymbol{z})} \exp\left[-\frac{1}{2}\sum_m (2\bar{n}_m+1)|A_m(\boldsymbol{z}) - A_m(\boldsymbol{z}')|^2\right]. \tag{S75}$$

This expression is used for the four target-spin basis branches in the numerical validation.

For comparison, we also use the two-target closure proxy

$$D = \sum_m (2\bar{n}_m+1)(|\alpha_{im}|^2 + |\alpha_{jm}|^2) \tag{S76}$$

for which, in general,

$$e^{-D} \neq C_z. \tag{S77}$$

Equality requires the weighted ion-i and ion-j displacement norms to satisfy the corresponding symmetry condition; it is not an identity of the conditional-Ramsey protocol.

S4.3 Parity analysis and phase extraction

The scanned analysis pulse uses the laboratory phase convention

$$R_i(\pi/2, -\varphi) = \exp\left[-\frac{i\pi}{4}(\cos\varphi X_i - \sin\varphi Y_i)\right]. \tag{S78}$$

This sign convention gives Eq. (S74); using the opposite laboratory phase simply relabels the horizontal scan axis. Ion j may be measured directly in Z. For symmetric timing, the equivalent analysis mapper $A_j = R_j(\pi/2, -\pi/2)H_j$ obeys $A_j^\dagger Z_j A_j = Z_j$ and leaves the parity formula unchanged. From the four two-ion populations,

$$\Pi_z(\varphi) = P_{00} + P_{11} - P_{01} - P_{10} = \langle Z_i Z_j \rangle. \tag{S79}$$

Branch correction by the known z gives

$$\widetilde{\Pi}_z = z\Pi_z = -C_z \sin(\varphi + 2z\Phi_{ij} - \vartheta_z^{\mathrm{mot}}), \tag{S80}$$

We fit the fringe as $\widetilde{\Pi}_z(\varphi) = B_z + C_z\cos(\varphi - \delta_z)$ with $C_z \geq 0$, where B_z is the fitted parity offset. In the ideal offset-free model, $B_z = 0$ and $\delta_z = -2z\Phi_{ij} + \vartheta_z^{\mathrm{mot}} - \pi/2$ modulo 2π. For any positive period P, we use the principal-branch convention

$$\mathrm{wrap}_P(x) = x - P\left\lfloor \frac{x + P/2}{P} \right\rfloor \in [-P/2, P/2). \tag{S81}$$

The fitted branch phases therefore give

$$\widehat{\Phi}_{ij} = \frac{1}{4}\,\mathrm{wrap}_{2\pi}(\delta_- - \delta_+ - \vartheta_-^{\mathrm{mot}} + \vartheta_+^{\mathrm{mot}}). \tag{S82}$$

The result is defined modulo $\pi/2$ because the overlap-corrected fringe difference is $4\Phi_{ij}$ modulo 2π. A continuous calibration sweep fixes the unwrap. Common analysis phase, branch-independent Z_i

frame error, and state-independent optical phase cancel in $\delta_- - \delta_+$; branch-dependent frame errors and $\vartheta_z^{\mathrm{mot}}$ do not. The latter vanishes for closed conditional trajectories and otherwise requires calculation or independent calibration.

For scrambled control, averaging fitted phases is not valid. We distinguish two physical implementations. In the shot-random implementation every detected shot draws an independent phase program, whereas a fixed-codebook implementation repeatedly samples one finite set $\mathcal{C}_R$ of R stored programs. Their exact coherent phasors and reduced channels are

$$\begin{aligned} \mathcal{Q}_z^{\mathrm{shot}} &= \mathbb{E}_r\left[C_{z,r}e^{i(2z\Phi_{ij,r}-\vartheta_{z,r}^{\mathrm{mot}})}\right], \qquad & \mathcal{M}^{\mathrm{shot}} &= \mathbb{E}_r[\mathcal{M}_r], \\ \mathcal{Q}_z^{(\mathcal{C}_R)} &= \frac{1}{R}\sum_{r\in\mathcal{C}_R} C_{z,r}e^{i(2z\Phi_{ij,r}-\vartheta_{z,r}^{\mathrm{mot}})}, \qquad & \mathcal{M}^{(\mathcal{C}_R)} &= \frac{1}{R}\sum_{r\in\mathcal{C}_R}\mathcal{M}_r. \end{aligned} \tag{S83}$$

Here $\mathcal{M}_r$ is the exact reduced-spin channel multiplier, equivalently its Choi representation. The observable fringe is $\widetilde{\Pi}_z(\varphi) = -\operatorname{Im}[e^{i\varphi}\mathcal{Q}_z]$. Thus $|\mathcal{Q}_z|$ is the ensemble-coherent fringe contrast and $\arg \mathcal{Q}_z$ is the ensemble fringe argument. Neither a fitted phase nor a motional correction is averaged separately.

Supplementary Table S8: Boundary-phase rules in the proposed reduced-model test.

Rule	Hardware implementation	Expected parity observable	Reduced-model test
continuous	DDS phase advances with laboratory time through power-off gaps	reproducible $\delta_- - \delta_+$ at the calibrated selected-pair phase	inter-window phase reference
reset	fixed DDS phase word reloaded at every active window	deterministic fringe redirection with the same envelope	tests boundary-quadrature dependence
scrambled, shot-random	independent uniform window phases on every detected shot	reduced ensemble-coherent fringe component	primary coherence-suppression test
scrambled, fixed codebook	randomized replay of one specified R-program codebook	codebook-dependent coherent phasor and channel	finite-program implementation diagnostic
gap-frozen-equivalent	next-window phase word omits dark-gap advance	deterministic shift from continuous with unchanged force envelope	tests memory through dark gaps

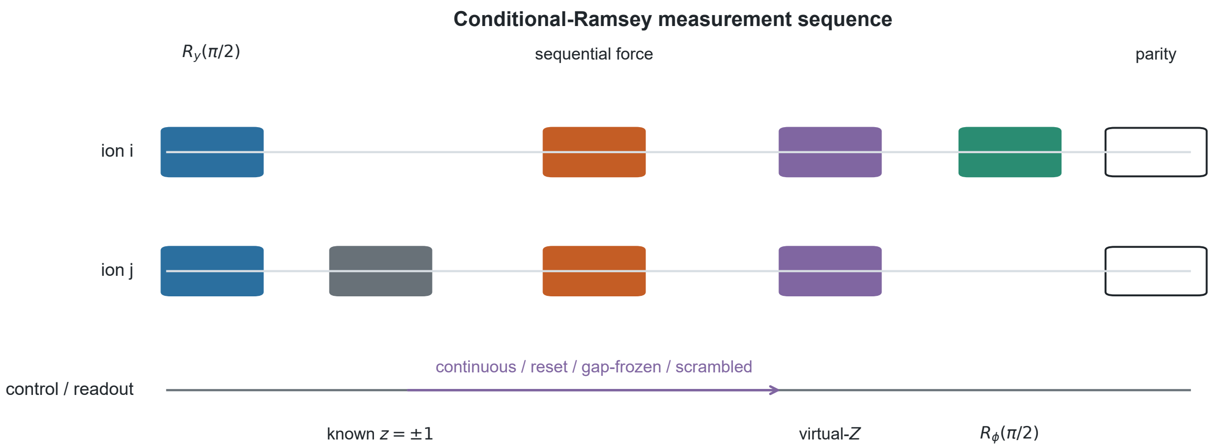

Supplementary Figure S2: Proposed conditional-Ramsey parity sequence for testing the reduced boundary-phase model. The experiment starts from $|++\rangle$, maps ion j to the two known Z branches, applies the same non-overlapping sequential force envelope, removes calibrated local Z phases by virtual-frame updates, and scans the analysis phase on ion i. The two Ramsey arms terminate at $A_{0,z,m}$ and $A_{1,z,m}$, and their separation $\Delta\alpha_{z,m}$ fixes the exact thermal contrast. The branch-fringe difference extracts Φ_{ij} through Eq. (S82) after the motional overlap phases are subtracted. This is a proposed measurement sequence and not an experimental state-characterization result.

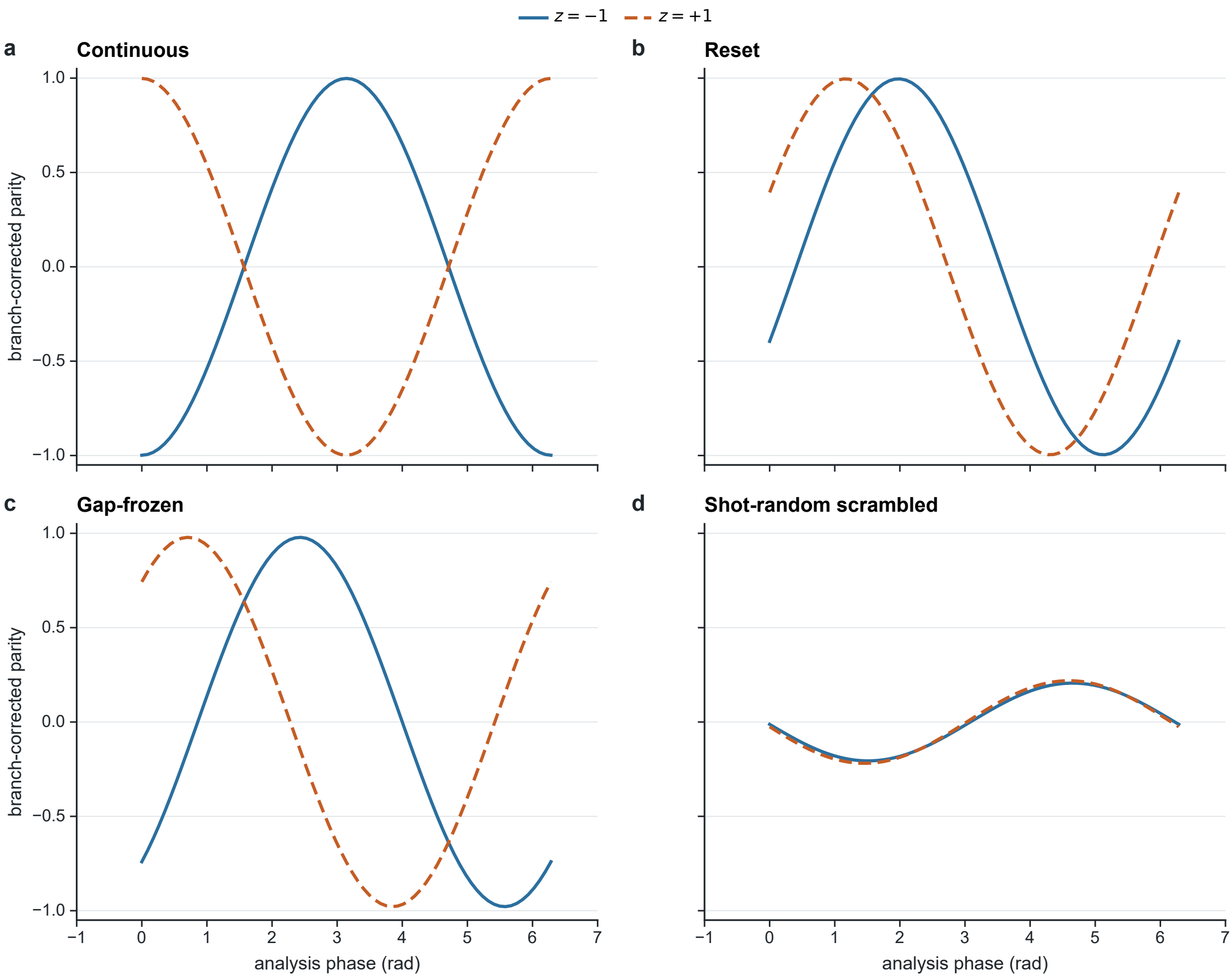

Supplementary Figure S3: Exact conditional-Ramsey parity traces for the measurable matched-envelope protocol. Columns show continuous, reset, gap-frozen, and shot-random scrambled controls under one common optical envelope and force calibration. Every trace uses the exact thermal conditional-displacement contrast in Eq. (S73); e^{-D} is not used as a visibility. The scrambled traces use the pooled 131072-program Monte Carlo estimate of Eq. (S83); they are not based on a fitted-phase average. Reset and gap-frozen preserve measurable contrast for this selected envelope; low-contrast schedules remain separate contrast-loss tests and are reported independently.

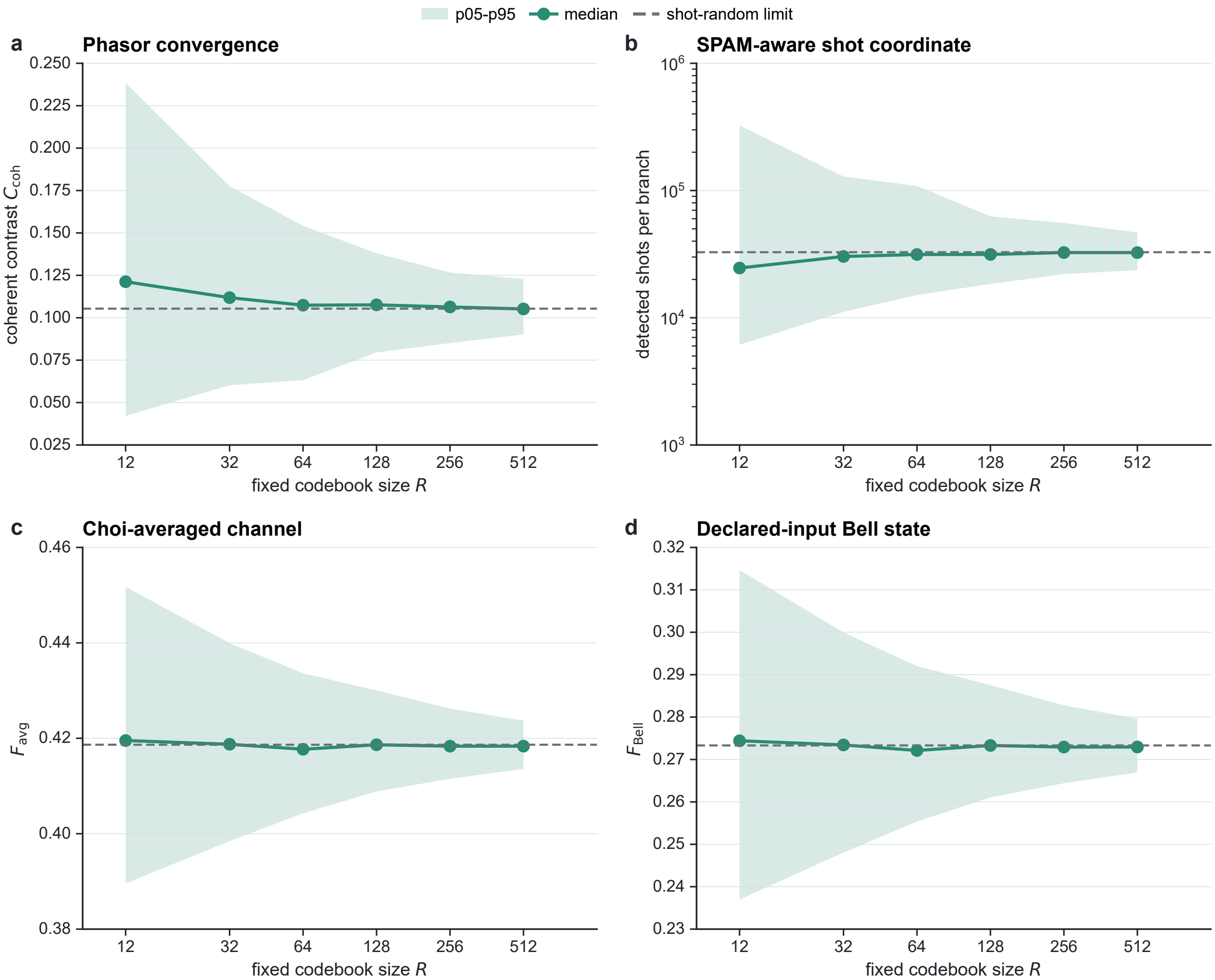

Supplementary Figure S4: Convergence of fixed-codebook scrambled controls to the shot-random ensemble. For each $R = 12, 32, 64, 128, 256, 512$, markers show the median across 256 independently seeded codebooks and bars show the p05–p95 codebook interval. Dashed lines give the pooled shot-random limit from 131072 independent phase programs. Channel quantities are calculated after averaging the complete reduced-channel multiplier, not by averaging fitted phases. The result for fixed codebook 0 at $R = 12$ illustrates codebook-to-codebook variation and is not the ensemble estimate.

Supplementary Table S9: Exact matched-envelope conditional-Ramsey and channel diagnostics. C_z is the mean exact thermal branch contrast, C_{coh} is the deterministic or scrambled coherent-phasor contrast, Δ_{cont} is the phase separation modulo $\pi/2$, and $\Delta\vartheta_{\mathrm{mot}}$ is the branch overlap-phase difference. $F_{\mathrm{avg}}^{-\pi/4}$ uses the specified target, whereas $F_{\mathrm{avg}}^{\mathrm{own}}$ uses each deterministic control's own pair phase and therefore does not make the control an alternative target gate.

Rule	Role	Φ_{ij} (rad)	C_z	C_{coh}	Δ_{cont} (rad)	$\Delta\vartheta_{\mathrm{mot}}$ (rad)	$N_{0.02}$	$F_{\mathrm{avg}}^{-\pi/4}$	$F_{\mathrm{avg}}^{\mathrm{own}}$
continuous	high-contrast reference	−0.785398	0.998439	0.998439	0.000000	0.001098	314	0.998751	0.998751
reset	phase-redirection test	−1.366828	0.996144	0.996144	0.581429	0.001256	315	0.756541	0.996925
gap-frozen	phase-redirection test	2.000099	0.978509	0.978509	0.356095	0.003637	327	0.887876	0.983013
scrambled	shot-random coherent-component suppression	n/a	0.191042	0.105361	n/a	n/a	30187	0.418649	n/a

S4.4 SPAM model and Fisher-information analysis

For equal exact branch contrast C and N optimally placed detected shots per branch, the known-contrast, zero-offset, single-operating-point binomial Fisher estimate gives

$$\sigma_\Phi \simeq \frac{1}{2\sqrt{2}\,C\sqrt{N}}. \tag{S84}$$

For unequal native branch contrasts C_- and C_+, the ideal quadrature Fisher estimate generalizes to

$$N_{0.02} = \frac{C_-^{-2} + C_+^{-2}}{16(0.02)^2} \tag{S85}$$

shots per branch. This expression assumes that the contrast, parity offset, analysis phase, and motional-overlap correction are known. It is a useful optimal-point coordinate, but it is not the uncertainty of a complete fringe fit. For the selected envelope, continuous, reset, and gap-frozen have exact contrasts 0.998439, 0.996144, and 0.978509. Reset redirects the phase by 0.581429 rad and has branch overlap-phase difference 0.001256 rad; gap-frozen redirects it by 0.356095 rad with overlap-phase difference 0.003637 rad. Both are therefore phase-redirection tests for this envelope. The shot-random scrambled rule instead has native branch-mean contrast 0.191042 and coherent ensemble contrast 0.105361. The corresponding 30187-shot value is calculated from the coherent phasor rather than a mean fitted phase; because the ensemble contrast is strongly suppressed, it is reported only as a descriptive coordinate. Across fixed codebooks, the median coherent contrast changes from 0.121242 (p05–p95 0.042096–0.238514) at $R = 12$ to 0.105177 (0.090134–0.122784) at $R = 512$. For fixed codebook 0 at $R = 12$, $C_{\mathrm{coh}} = 0.212506$ and the corresponding estimate is 6940 ideal shots per branch.

To expose SPAM dependence without assigning unmeasured single-ion error rates, we adopt an effective parity-level model,

$$\begin{aligned} C_z^{\mathrm{eff}} &= C_z^{\mathrm{coh}}\,(1 - 2e_{\mathrm{prep}}^{\Pi})(1 - 2e_{\mathrm{ro}}^{\Pi}), \\ \mu_{z,k} &= b + C_z^{\mathrm{eff}}\cos(\varphi_k + \epsilon_a - \delta_z), \qquad p_{z,k}^{(\pm)} = \frac{1 \pm \mu_{z,k}}{2}. \end{aligned} \tag{S86}$$

Here e_{prep}^{Π} and e_{ro}^{Π} are phenomenological parity-contrast coordinates. They are not per-ion preparation or readout probabilities and cannot be separated using one parity fringe without external calibration. For deterministic controls $C_z^{\mathrm{coh}} = C_z$; for scrambled control it is the magnitude of the converged ensemble phasor $\mathcal{Q}_z$. The analysis-phase shift ϵ_a and parity offset b are likewise model coordinates rather than measurements.

For one optimally placed shot, the known-parameter information for branch phase δ_z is

$$\mathcal{I}_{\delta,z}^{\mathrm{op}} = \frac{(C_z^{\mathrm{eff}})^2\cos^2\epsilon_a}{1 - [b - C_z^{\mathrm{eff}}\sin\epsilon_a]^2}. \tag{S87}$$

The branch-phase Fisher information contains no extra factor of four. The 1/4 conversion from the difference of the two fitted branch phases to Φ_{ij} appears in Eq. (S82) and produces the factor

1/16 in the pair-phase variance below. For a uniform grid of K analysis phases and nuisance vector $\boldsymbol{\theta}_z = (\delta_z, C_z^{\mathrm{eff}}, b)$, the Fisher matrix per detected shot is

$$F_{ab}^{(z)} = \frac{1}{K} \sum_{k=1}^{K} \frac{\partial_a \mu_{z,k}\, \partial_b \mu_{z,k}}{1 - \mu_{z,k}^2}. \tag{S88}$$

With equal detected counts N in the two known-Z branches, the nuisance-aware bound is

$$\mathrm{Var}(\widehat{\Phi}_{ij}) \geq \frac{[(F^{(-)})^{-1}]_{\delta\delta} + [(F^{(+)})^{-1}]_{\delta\delta}}{16N}. \tag{S89}$$

The single-parameter grid bound replaces each inverse-matrix element in Eq. (S89) by $1/F_{\delta\delta}^{(z)}$. Both calculations assume that the analysis-phase grid is calibrated and that $\vartheta_z^{\mathrm{mot}}$ is known or independently corrected. A free common analysis-phase offset is exactly degenerate with the fitted fringe phase and therefore cannot be added as an independent nuisance parameter without an external phase reference.

For the coordinates $e_{\mathrm{prep}}^{\Pi} = 0.010$, $e_{\mathrm{ro}}^{\Pi} = 0.010$, $\epsilon_a = 0.030$ rad, and $b = 0.020$, Table S10 compares the known-(C, b) grid bound, the joint phase/contrast/offset bound, and direct finite-shot fitting. The Monte Carlo column rescales the simulated variance to the target $\sigma_\Phi = 0.02$ rad; each entry uses 4000 independent binomial data sets on the same 12-point grid.

Supplementary Table S10: SPAM and phase-grid Fisher validation. All entries are detected, accepted parity outcomes per known Z branch. The scrambled row uses the converged shot-random ensemble phasor.

Rule	Known C, b CRB	Joint δ, C, b CRB	Monte Carlo equivalent	$\sigma_\Phi^{\mathrm{MC}}$ (rad)
continuous	444	445	450	0.020093
reset	438	439	470	0.020681
gap-frozen	467	468	495	0.020559
scrambled, shot-random	65271	65271	64092	0.019818

For the uniformly sampled grid, nuisance parameters add only a small penalty; most of the increase relative to the single-operating-point estimate arises because detected shots are distributed across a complete fringe. The finite-shot simulations jointly fit phase, contrast, and offset by binomial Fisher scoring and reproduce the analytic target within the numerical spread in the source data. The scrambled-control result uses the converged shot-random C_{coh} rather than a single 12-program codebook.

Every count in Table S10 denotes a detected, accepted parity outcome entering the phase-grid fit. If the acceptance probability is p_{acc}, the number of experimental attempts per branch is $N_{\mathrm{attempt}} = N_{\mathrm{detected}}/p_{\mathrm{acc}}$. An elapsed-time estimate additionally requires a supplied cycle time, $T = N_{\mathrm{attempt}} T_{\mathrm{cycle}}$. Neither p_{acc} nor T_{cycle} is available in the present model, so no attempt count or experimental duration is reported. The phase-drift and switching-jitter scans give maximum pair-phase shifts of 0.000986 and 0.631421 rad, respectively; these are model-level sensitivity coordinates rather than hardware tolerances.

Phase redirection is assessed only when the exact contrast is measurable and the motional-overlap phase is small or independently corrected; strong contrast loss is analyzed separately. The four control rules and two known-Z branches are randomized within each eight-block supercycle to reduce sensitivity to slow drift.

The two-target closure diagnostic is

$$D = \sum_m (2\bar{n}_m + 1)(|\alpha_{im}|^2 + |\alpha_{jm}|^2). \tag{S90}$$

It remains useful for ranking two-target closure burden, but e^{-D} is not the native conditional-Ramsey visibility and is never substituted for C_z in Figs. S3 and S4, Table S9, or the shot estimates.

S4.5 Direct finite-Fock validation

The analytic trace is independently checked with one- and two-mode thermal states in finite Fock spaces. For each known branch z, the calculation constructs the complete conditional spin–motion unitary

$$U_z = |0\rangle\langle 0|_i \otimes e^{-iz\Phi_{ij}} \prod_m D_m(A_{0,z,m}) + |1\rangle\langle 1|_i \otimes e^{+iz\Phi_{ij}} \prod_m D_m(A_{1,z,m}), \tag{S91}$$

propagates $|+\rangle\langle +|_i \otimes \rho_{\mathrm{th}}$, traces out motion, and applies Eq. (S78). The one-mode case uses a cutoff of 18 and the two-mode case uses cutoffs of 14 and 16, with normalized thermal tails. Across 65 analysis phases and both z branches, the maximum analytic-versus-direct fringe discrepancy is 1.67×10^{-15}, the maximum contrast discrepancy is 1.33×10^{-15}, and the overlap-corrected extracted-phase discrepancy is zero at the reported precision. The 10^{-9} validation threshold is therefore passed for both cases. The authors' working reproducibility tree records the source values and independent finite-dimensional validation under the internal filename `data/exact_ramsey_fock_validation.csv`. These checks validate the conditional-displacement algebra; they are not apparatus simulations.

S4.6 Exact two-qubit reduced-channel validation

For the four computational branches $\boldsymbol{z} = (z_i, z_j)$, with all nontarget ions fixed in the specified $Z = -1$ states, define

$$A_m(\boldsymbol{z}) = \beta_m + z_i\alpha_{im} + z_j\alpha_{jm}, \qquad \Theta(\boldsymbol{z}) = \gamma + \lambda_i z_i + \lambda_j z_j + \Phi_{ij} z_i z_j. \tag{S92}$$

After the deterministic local-Z correction, tracing a thermal motional state gives the exact reduced-spin map

$$\begin{aligned} \rho_{\boldsymbol{z},\boldsymbol{z}'}(T) = \rho_{\boldsymbol{z},\boldsymbol{z}'}(0) \exp&\left\{ i \left[\Theta_c(\boldsymbol{z}) - \Theta_c(\boldsymbol{z}') + \mathrm{Im} \sum_m A_m(\boldsymbol{z}')^* A_m(\boldsymbol{z}) \right] \right\} \\ &\times \exp\left[-\frac{1}{2} \sum_m (2\bar{n}_m + 1) |A_m(\boldsymbol{z}) - A_m(\boldsymbol{z}')|^2 \right]. \end{aligned} \tag{S93}$$

The map is evaluated as a Schur multiplier and independently represented as a 16×16 superoperator and normalized Choi matrix. Trace preservation, Hermiticity preservation, complete positivity, the zero-force identity limit, and the closed-loop unitary limit are checked numerically. The largest channel-structure residual across the evaluated cases is 1.09×10^{-16}, and direct one- and two-mode finite-Fock calculations agree with the analytic channel to 5.22×10^{-15}. In the authors' working reproducibility tree, the complete matrices and validation fields are recorded under `data/two_qubit_channel_metrics.csv` and `data/two_qubit_choi_validation.csv`.

Supplementary Table S11: Selected exact reduced-channel metrics. Average gate fidelity is relative to $\exp[-i(\pi/4)Z_iZ_j]$ after deterministic local-Z correction. Bell-state fidelity uses the specified $|++\rangle$ input and analysis convention.

Case	average gate fidelity	Bell-state fidelity
Unshaped continuous	0.910319	0.887898
Optimized continuous	0.999927	0.999908
Passband-aware continuous	0.999995	0.999994
Idealized single-projector limit	0.999927	0.999908

The common displacement β_m cancels from every branch difference $A_m(\boldsymbol{z}) - A_m(\boldsymbol{z}')$ and therefore does not alter the Gaussian damping factor. When differential trajectories remain open, it can enter the Weyl overlap phase in Eq. (S93). Reset, gap-frozen, and scrambled controls are included in the complete nine-case table even when their target-operation fidelities are low; the scrambled channel is averaged at the Choi-matrix level rather than by averaging fitted phases.

S4.7 Spectator-superposition extension

The fixed-Z protocol above does not by itself describe a spectator prepared in a coherent superposition. For one selected spectator s, with all remaining spectators fixed at $Z = -1$, we therefore include the eight branches $\boldsymbol{z} = (z_i, z_j, z_s)$ and use

$$A_m(\boldsymbol{z}) = \beta_m + z_i\alpha_{im} + z_j\alpha_{jm} + z_s\alpha_{sm} + A_{\text{fixed},m}, \qquad \Theta(\boldsymbol{z}) = \gamma + \sum_q \lambda_q z_q + \sum_{q<r} \Phi_{qr} z_q z_r. \quad \text{(S94)}$$

After tracing the thermal motion, the exact three-spin matrix elements are

$$\begin{aligned} \rho_{\boldsymbol{z},\boldsymbol{z}'}(T) = \rho_{\boldsymbol{z},\boldsymbol{z}'}(0) \exp\left\{ i \left[\Theta_c(\boldsymbol{z}) - \Theta_c(\boldsymbol{z}') + \operatorname{Im} \sum_m A_m(\boldsymbol{z}')^* A_m(\boldsymbol{z}) \right] \right\} \\ \times \exp\left[-\frac{1}{2} \sum_m (2\bar{n}_m + 1) |A_m(\boldsymbol{z}) - A_m(\boldsymbol{z}')|^2 \right], \end{aligned} \quad \text{(S95)}$$

where Θ_c includes the fixed target local-Z frame calibrated for spectator $|0\rangle$. Tracing s gives the induced target channel. Because the Hamiltonian is diagonal in Z_s, that target channel depends on the spectator Z populations; spectator coherence instead remains visible in target–spectator mutual information and negativity before the final spectator trace. Thus $|+\rangle_s$ and a maximally mixed spectator have the same target population-averaged channel in this model, but only $|+\rangle_s$ can retain coherent target–spectator entanglement.

The representative targets are one-based ions 2 and 4. Ion 3 maximizes directed target-to-spectator leakage, and the distinct ion 5 is the next-largest target–spectator-ZZ case under the same scale-0.006, seed-90000 directed matrix used in the control-parameter transfer scan. The 48 records compare phase-programmed and passband-aware waveforms under zero, scalar, and directed leakage for spectator $|0\rangle$, $|1\rangle$, $|+\rangle$, and the maximally mixed state. Zero leakage leaves the unforced spectator factorized to numerical precision. Finite leakage produces at most 1.182×10^{-3} bits of mutual information and 6.102×10^{-3} negativity for the specified $|+\rangle$ cases, with a maximum matching-row target Bell-fidelity loss of 1.527×10^{-4}. These are exact model-level channel estimates, not measured fidelities.

For spectator $|0\rangle$ or $|1\rangle$, $\Phi_{is}z_iz_s + \Phi_{js}z_jz_s$ is a deterministic target local phase; a spectator-state-conditioned virtual-Z update removes that coherent part. For $|+\rangle_s$, the same terms generate unwanted target–spectator entanglement and no target-only local frame can remove it. The appropriate controls are spectator initialization, suppression of the leakage-induced force, or an echo/cancellation sequence that reverses the target–spectator interaction. The authors' working reproducibility tree records the complete channels, target fidelities, mutual information, negativity, local-phase splits, leakage-induced target-force overlap, and numerical residuals under `data/spectator_superposition_channel.csv`, with an internal compact visualization named `figures/spectator_superposition_channel.pdf`.

The four control rules and both z branches should be interleaved while the DDS phase word, AOD switching transient, dark-gap extinction, and leakage matrix are monitored. Under the matched envelope, continuous control should reproduce the calibrated phase, reset and gap-frozen control should produce deterministic phase and/or closure changes, and scrambled control should suppress the coherent component. Statistically indistinguishable phase and contrast across all four controls would be inconsistent with the reduced boundary-phase model under the stated corrections.

S5. Chain-Size and Mode-Spectrum Scan

The representative scan covers 5-, 10-, and 20-ion chains, two parameterized spectra, and near, middle, and far target pairs. Thirteen of 18 continuous-rule conditions reach the requested branch and five reach the opposite sign, confirming that branch selection remains pair and spectrum dependent. Mode-resolved decompositions and the complete trace table were generated in the authors' working source-data tree.

S6. Sequential-versus-Simultaneous Resource Trade-Off

The comparison is constrained resource accounting, not an architecture ranking. A spatial retargeting event changes the addressed target set, a segment transition changes amplitude or phase without necessarily moving a beam, and a dark gap has zero intended target force. Under these definitions, simultaneous pulse boundaries are not retargeting events.

For the dimensionless target envelopes $u_q(t)$ and reported force scale f, we define

$$\mathcal{I}_2 = \int dt \sum_{q=i,j} |f u_q(t)|^2, \qquad \eta_\Phi = \frac{|\Phi_{ij}|}{\mathcal{I}_2}.$$

This normalization compares phase per squared model control action for a fixed mode spectrum; it does not include beam waist, optical power, multilevel scattering, or wall-plug conversion. The four anchors compare fixed peak force, fixed $\mathcal{I}_2$, and independent target-phase calibration. After $-\pi/4$ calibration, the sequential and simultaneous force scales are 3.7704 and 1.9409, and the simultaneous phase efficiency is 1.826 times larger. The sequential schedule is therefore not force saving in this representative model.

The calibrated schedules share the same 240-μs duration. Their active times, closure coordinates, spectator burden, event counts, and approximation-screening fields are reported in Fig. S5 and the source CSV.

The fixed-scattering entry is bookkeeping only: without a force-to-optical-power map, it cannot identify which branch meets a physical scattering budget after recalibration. Branch definitions, duration sweeps, and validation fields were generated in the authors' working source-data tree.

S7. Additional Pair-Resolved and Robustness Diagnostics

The authors' working source-data tree contains additional pair-resolved, force-quadrature, noise, crosstalk, mode-resolved, and two-dimensional robustness diagnostics. These data extend the aggregate results presented in Sections S5, S6, S14–S17 without introducing additional model assumptions.

S8. Numerical and Internal-Consistency Checks

The numerical and internal-consistency checks cover the disjoint-window phase identity, unit conversion, real-force/RWA agreement, projector-force reduction, exact conditional contrast, finite-Fock and Choi comparisons, physical normal modes, waveform constraints, all-pair completeness, reduced-Hamiltonian approximation screening, independent control-resource burdens, and apparatus-interface behavior. The waveform checks enforce signed $-\pi/4$ calibration, zero target overlap, zero hidden gap force, no simultaneous illumination, peak-force and phase-increment bounds, and the mode-resolved projector relation $\beta_m = \alpha_{im} + \alpha_{jm}$. The causal-kernel tests independently require a zero equal-time target product and agreement among analytic, direct-integration, and Magnus-recurrence results.

The optical interface is also checked for wavelength consistency, E1/E2 formula selection, branching-ratio normalization, missing-input refusal, and separation of bookkeeping, user-supplied, and measured-comparison fields. In the authors' working tree, a consolidated summary is stored as `data/validation_summary.csv` and is available upon reasonable request. These tests establish numerical consistency within the specified models; they do not validate an experimental apparatus or supply missing atomic data.

S9. ZZ, CZ, CNOT, and Bell-Parity Logic

A pure ZZ interaction adds computational-basis phases and does not convert $|00\rangle$ directly into a Bell state. Bell-parity readout therefore requires superposition preparation, the ZZ/CZ-equivalent

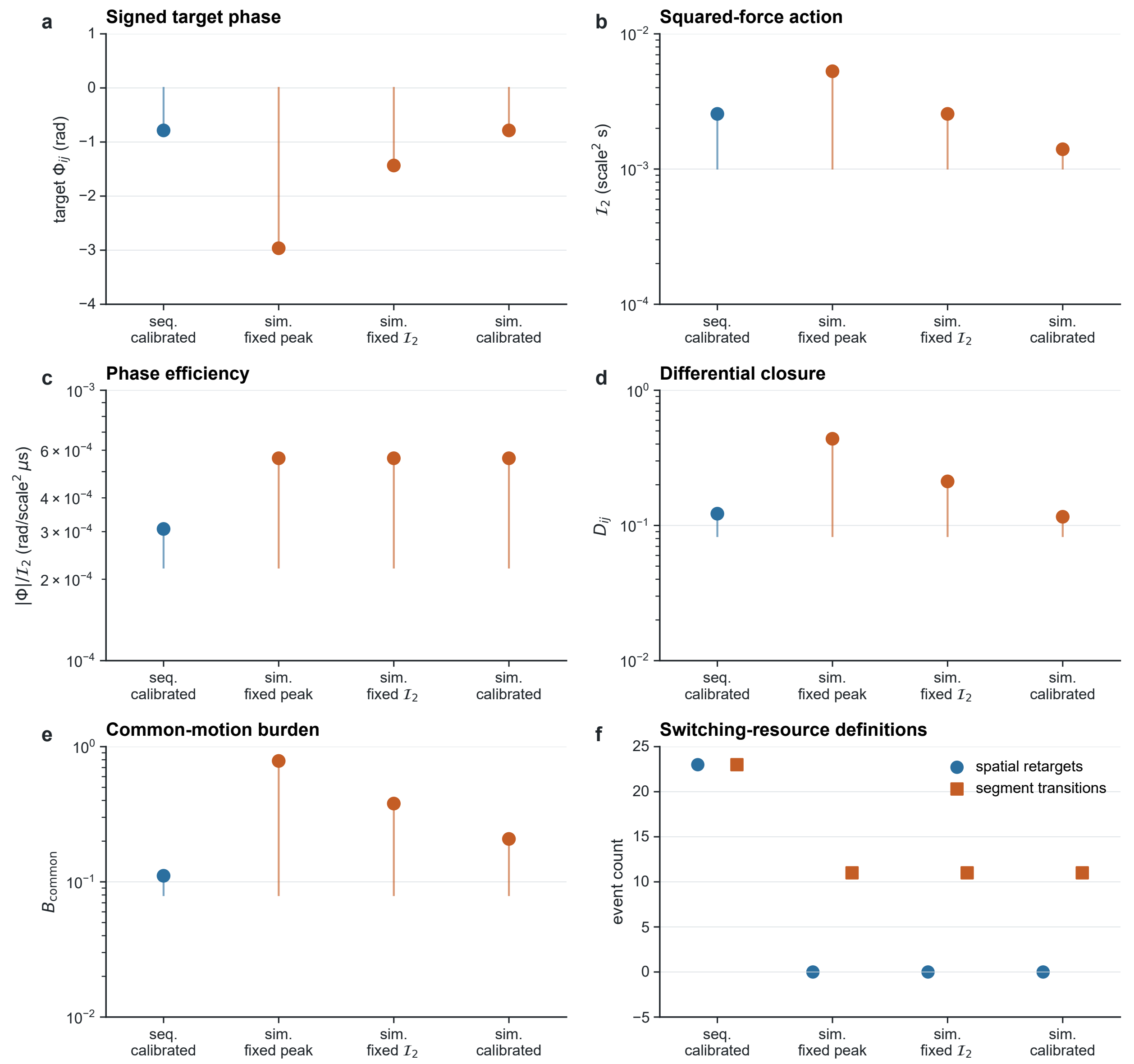

Supplementary Figure S5: Detailed sequential-versus-simultaneous normalization comparison. The four anchors compare fixed per-channel peak force, fixed squared-force action $\mathcal{I}_2$, and independent target-phase calibration. The panels show signed phase, $\mathcal{I}_2$, phase efficiency, separated spatial-retargeting/segment-transition counts, differential closure, and common-motion burden. Peak force, active time, duration, spectator ZZ, approximation-screening fields, control-resource burdens, and fixed-rate scattering bookkeeping are reported in the text and source CSV; no physical-scattering ranking is inferred.

phase, calibrated local-Z frames, and analysis rotations; a CNOT construction additionally uses target Hadamards. Section S4 gives the corresponding Ramsey/parity sequence and phase-extraction formula.

S10. Organization of the Source Data

The authors' working source data are organized into finite-window theory, Ramsey and channel outputs, spectator analysis, normal-mode calculations, waveform optimization, many-ion scans, apparatus-interface grids, and figure data. Bookkeeping quantities and user-supplied atomic-data estimates are confined to the optical interface described in Section S3. Section S18 gives the source-data and code-availability statement.

S11. Parameter Sources and Auxiliary Ranking Field

Baseline inputs are classified as hardware-motivated, representative, target, stress-test, or numerical-threshold values. Device-level use requires calibrated mode, phase, leakage, and noise inputs. The auxiliary field `estimated_error_proxy` is used only for ordering within the model and is neither a fidelity nor a calibrated error model.

S12. Regime Comparison and Resource Interpretation

The comparison below follows the Methods and reported equations of Hou *et al.* [2], who used a crossed-AOD experiment with alternating single-ion Raman-force segments separated by dark switching intervals.

In our notation, each segment is a window W_{jp} and the published displacement-commutator phase maps directly to the ordered window-kernel sum in Proposition 1. This experiment provides an experimental reference point for non-simultaneous phase generation. Here, the boundary phase is treated as an independent control variable and analyzed through closure, robustness, and transfer diagnostics.

Supplementary Table S12: Relation to the Hou alternating-addressing experiment. The comparison narrows the present contribution to boundary-phase controls and transfer diagnostics.

Criterion	Hou *et al.*	Present work	Interpretation
Alternating addressing demonstrated?	Yes, experimentally for diagonal pairs	Yes, as a zero-overlap theory/simulation framework	Experimental reference point for alternating addressing
Experimental?	Yes	No; theory and simulation framework	Hou-like controls here are theoretical re-analysis only
Boundary phase isolated as independent control?	Phase modulation is used for closure and entangling phase	Boundary phase is isolated as phase-clock coherence	Main narrowed contribution
Reset control?	Not separately analyzed in Ref. [2]	Explicit theoretical control	Additional theoretical control considered here
Scrambled control?	Not separately analyzed in Ref. [2]	Seeded ensemble theoretical control	Tests coherent boundary reference
Gap-frozen control?	Not separately analyzed in Ref. [2]	Artificial counterfactual control	Tests phase advance through dark gaps
Zero-leakage hidden-force exclusion?	Low crosstalk reported experimentally	Explicit zero-leakage simulation and hidden-force exclusion	Separates commutator phase from residual simultaneous forcing
Passband-aware closure?	Not the focus of the reported alternating-sequence comparison	Drift-moment and worst-band diagnostics	Separates zero-drift closure from drift robustness
All-pair atlas?	Four-ion 2D experimental pairs	5/10/20/30-ion physical-chain design atlas	Design map, not hardware yield
Switching-phase response?	Switching separation and compensation are part of the experiment	Phase-step/chirp transfer maps	Transfer coordinate for another apparatus
Explicit rejection criterion?	Not framed as a boundary-phase model test	Phase-rule and hidden-force rejection criteria	Defines when the reduced model is rejected or incomplete

Simultaneous addressed gates rely on concurrent site-resolved forces; global and multi-tone gates rely on common fields and spectral shaping; cancellation protocols add calibrated compensating paths; and the present primitive relies on a retargetable channel with a stable inter-window phase reference and dark-gap extinction. These regimes carry different spectator, closure, and phase-calibration burdens. The quantitative comparison therefore fixes peak force, squared force action, duration, channel count, or target phase separately and does not imply a universal ranking or lower-power advantage.

S13. Dimensionless Control Coordinates

Supplementary Table S13: Dimensionless coordinates for transferring the design rule to another apparatus.

Coordinate	Representative scan axis	Use in a hardware implementation
$2\pi\delta_{\mathrm{res}}T_{\mathrm{seq}}$	residual AOD/AOM detuning stored in hertz	Sets the accumulated phase error from imperfect force-frequency compensation
$\delta_m\Delta_c$	center-to-center window delay	Controls the sign and magnitude of the near-resonant cross-window kernel together with the relative boundary phase
σ_ϕ	window phase noise	Measures randomization of the inter-window phase reference
$\delta_m\sigma_t$	switching-latency jitter	Converts timing jitter into near-resonant force-quadrature uncertainty for each mode
ϵ_{leak}	leakage force divided by addressed force	Bounds spectator ZZ and distinguishes true cross-window phase from residual simultaneous forcing
$(A_+ - A_-)/(A_+ + A_-)$, $\Delta\phi_{+-} \equiv \phi_+ - \phi_-$	positive/negative-frequency quadrature imbalance	Tests whether the reduced cosine-force assumption remains valid
$\Phi_{ij}^{(m)}$, dominance margin	exact mode-resolved symplectic phase	Certifies the total sign only when the strict dominant-mode inequality is satisfied
S_{ij}^{heur}	window-center short-window diagnostic	Provides a screening coordinate only; it is not an exact branch criterion

These coordinates are deliberately separated from experimental performance characterization. They are the variables that a second apparatus should report before comparing a measured phase-rule experiment with the present simulation model and reported numerical summaries.

S14. Physical Coulomb-Chain Normal-Mode Solver

S14.1 Baseline physical normal modes

The physical solver minimizes the symmetric one-dimensional Coulomb-plus-harmonic potential and diagonalizes the radial dynamical matrix. The inputs are an axial secular frequency of 180 kHz, a radial secular frequency of 2.50 MHz, ion mass 171 u, wavelength 435 nm, and effective radial wave-vector projection 0.78. The solver stores equilibrium positions, maximum force residual, radial frequencies, eigenvectors, Lamb–Dicke matrices, and model thermal occupations for each chain.

Supplementary Table S14: Physical normal-mode outputs. Values are simulation estimates for the declared trap model.

N	lowest radial mode (MHz)	highest radial mode (MHz)	pair count	max equilibrium residual
5	2.459	2.500	10	8.88×10^{-16}
10	2.359	2.500	45	1.78×10^{-15}
20	1.990	2.500	190	9.30×10^{-14}
30	1.261	2.500	435	6.93×10^{-14}

The physical spectra provide a self-consistent trap model rather than an apparatus-specific calibration. Parameterized linear and compressed spectra are included as comparison controls.

S14.2 Trap-parameter sensitivity and all-pair cost distributions

The baseline model is supplemented by the Cartesian scan $\omega_z/(2\pi) = 100, 150, 180, 250, 300$ kHz, $\omega_r/(2\pi) = 2.0, 2.5, 3.0, 3.5$ MHz, radial wave-vector projection $0.5, 0.78, 1.0$, and $N = 10, 20, 30$. Each valid set repeats the four-offset target-sign synthesis for all $i < j$ pairs and reports the radial-mode bandwidth, minimum spacing, signed and absolute Lamb–Dicke ranges, force-scale and displacement quantiles, within-cap fraction, and dominant-mode histogram. Non-positive radial Hessians are written as invalid records with the failing parameter combination and exception reason. The scan contains 150 stable and 30 invalid parameter sets; the stable subset comprises 29,355 pair rows. For interpretation, the same 180 parameter sets are separated into two direct Hamiltonian/Magnus calculations for the central nearest-neighbour pair of each chain. The fixed-schedule transfer scan holds the target mode at the lowest radial mode, uses $\mu - \nu_0 = 16$ kHz and a 2 μs gap, and tests the four specified target-sign boundary phases with scalar force calibration to the target phase. The mode-adapted scan evaluates the lowest, center-of-mass, and three strongest signed-coupling mode candidates, $\mu - \nu_m \in \{8, 16, 24\}$ kHz, gaps $\{1, 2, 4\}$ μs, the four boundary phases, and the same scalar force calibration. Every candidate is recomputed from the force Hamiltonian; no adaptation-gain scaling is used. The adapted output is a lower envelope over this finite grid, not a global optimum or measured apparatus performance.

Supplementary Table S15: Trap-sensitivity summary by chain size. Medians are taken over stable trap/projection sets.

N	stable/60	invalid/60	median cap fraction	median force scale	median D_{ij}
10	60	0	0.878	10.35	5.53
20	51	9	0.363	36.15	6.54
30	39	21	0.221	74.62	16.39

For the 150 stable trap sets, the fixed/adapted median force coordinates are 6.90/5.34, the differential-displacement coordinates are 0.797/0.154, and the exact conditional contrasts are 0.442/0.857. The median ratio of fixed to adapted objective is 4.04. All candidates preserve zero target-window overlap, zero dark-gap force, and no simultaneous illumination. These medians compare one pair geometry and one specified control grid; they do not establish all-pair scaling.

S14.3 Normal-mode convergence and thermal weighting

The normal-mode convergence study repeats every stable trap-set solve at dimensionless equilibrium tolerances 10^{-8}, 10^{-10}, and 10^{-12}. The equilibrium optimizer uses the analytic gradient, and the comparison records its residual, the analytic-Hessian minimum eigenvalue, the maximum relative radial-mode-frequency change, and the minimum eigenvector overlap against the strictest solution. One common acceptance rule is used for every chain size: residual $\leq 10^{-9}$, relative frequency change $\leq 10^{-8}$, and overlap ≥ 0.99999999. All 450 records pass; the observed maxima are 9.30×10^{-14} and 8.03×10^{-16}, and the minimum overlap is 0.9999999999999978.

For each stable fixed and adapted solution, the thermal comparison uses the mode-resolved α_{qm} and evaluates (i) unweighted closure, (ii) a uniform illustrative $\bar{n} = 0.475$, and (iii) Bose occupations $\bar{n}_m(T) = [\exp(\hbar\omega_m/k_{\mathrm{B}}T) - 1]^{-1}$ at 5 μK and 0.5 mK. Thus fixed-temperature weighting is performed mode by mode rather than by assigning the dominant-mode occupation to the total displacement. The temperatures and fixed occupation are simulation inputs, not measured cooling results.

S15. Sequential Waveform Synthesis and Motional Closure

S15.1 Common- and differential-closure optimization

The reduced optimization minimizes the target differential closure

$$D_{ij} = \sum_m (2\bar{n}_m + 1) \left(|\alpha_{im}|^2 + |\alpha_{jm}|^2\right). \tag{S96}$$

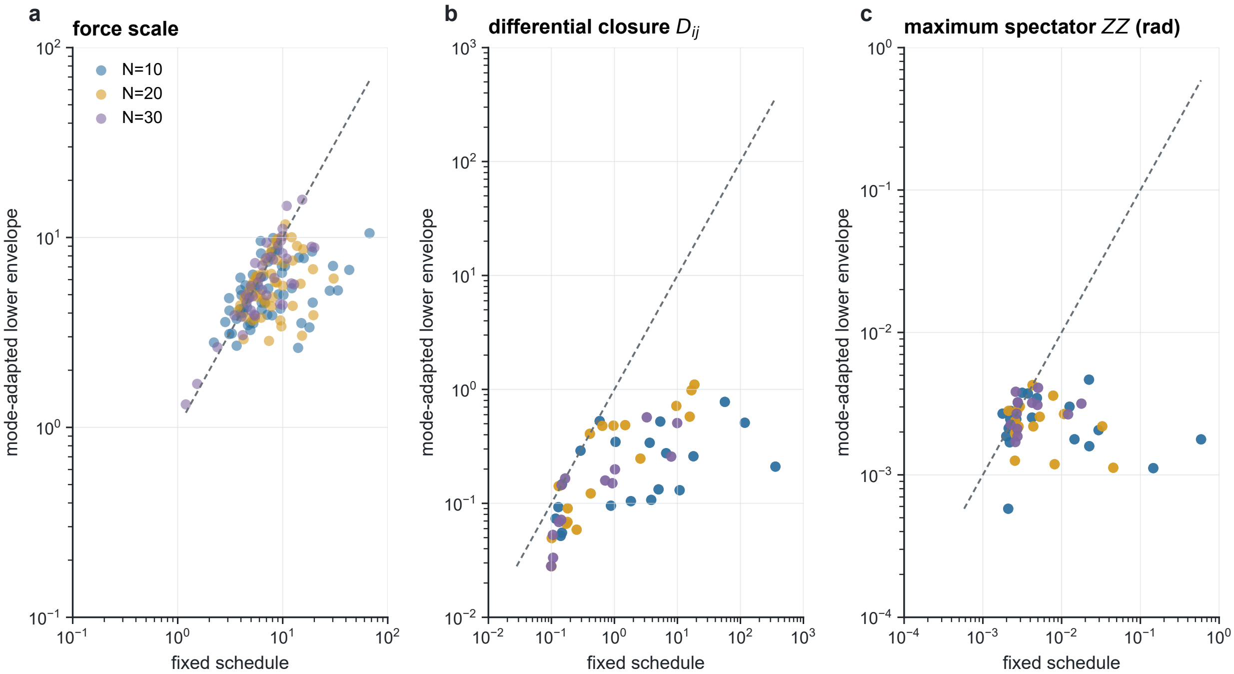

Supplementary Figure S6: Fixed-schedule transfer versus the mode-adapted lower envelope. Each point is one stable idealized trap set for the same central nearest-neighbour pair. The diagonal marks equal cost. The adapted ordinate is the best direct Hamiltonian/Magnus result on the specified mode, beat-note, gap, boundary-phase, and scalar-calibration grid; it is not a global optimum or measured hardware performance.

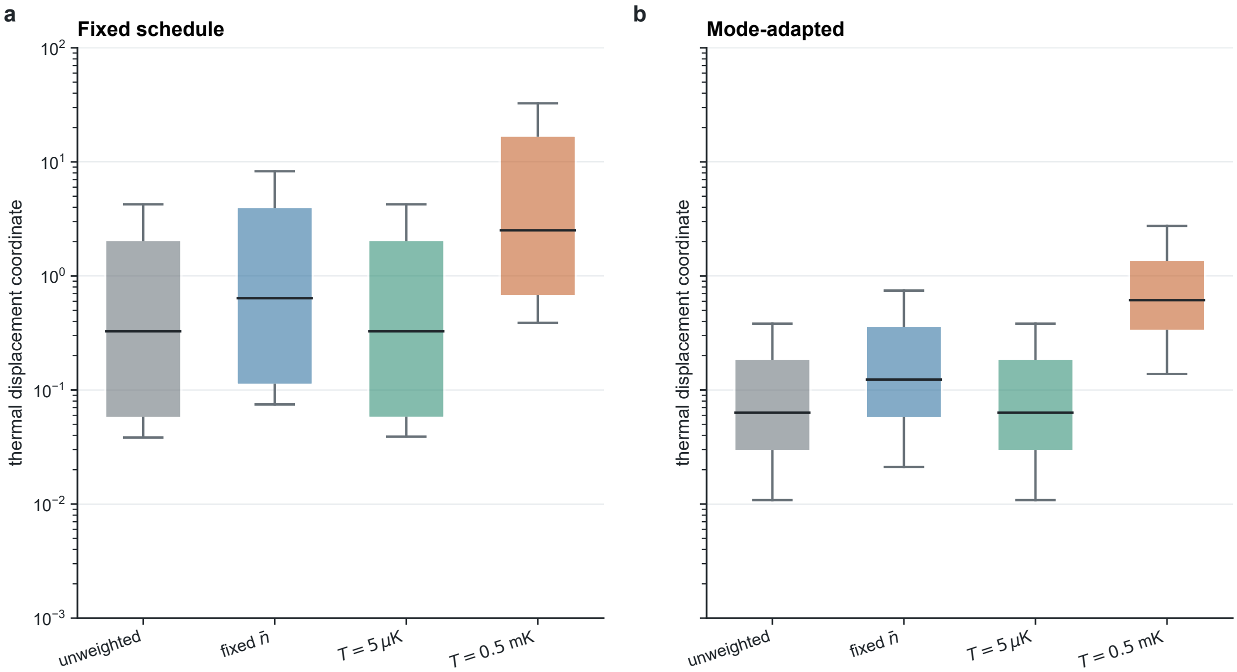

Supplementary Figure S7: Mode-resolved thermal-weighting effect. The same calculated displacements are shown without thermal weights, with uniform fixed $\bar{n}$, and with two illustrative fixed-temperature Bose occupations. The panels separate fixed-schedule and mode-adapted controls. Temperatures are model inputs, not apparatus measurements.

For the projector coupling adopted in the idealized reduction, the corresponding common-motion coordinate is

$$B_{\mathrm{common}} = \sum_m (2\bar{n}_m + 1)|\beta_m|^2, \qquad \beta_m = \alpha_{im} + \alpha_{jm} \tag{S97}$$

in the target-only, zero-leakage synthesis model. The second equality is checked mode by mode rather than assumed. We additionally penalize the RMS wrapped local phase of the targets. This phase is deterministic and may be tracked by virtual-Z frames, but a frame update does not close the common motional trajectory.

Three cases use the same six-parameter window-amplitude and bounded boundary-phase basis. Case A optimizes differential closure in the idealized single-projector model. Case B adds B_{common} and local-phase penalties. Case C uses the optimized differential force g_z while setting g_0 and the specified deterministic local-phase coordinate to zero in an ideal balanced-force construction. Case C is a resource limit, not a claim that a particular echo automatically cancels the identity force or that the 435 nm architecture implements a balanced force. All cases enforce zero target overlap, zero force in dark gaps, no simultaneous target illumination, $\Phi_{ij} = -\pi/4$, peak model-force scale below 8.0, and adjacent boundary-phase increments below 0.8 rad.

Supplementary Table S16: Idealized single-projector closure trade-off. Closure weights are not infidelities; the contrast is the exact thermal conditional-Ramsey result for the specified known-branch protocol.

Case	D_{ij}	B_{common}	local-Z RMS (rad)	force	peak	spectator ZZ (rad)	$C_{\mathrm{cond,min}}$	max absolute motion burden
A differential only	9.301×10^{-5}	1.509×10^{-4}	1.3510	2.6170	4.6622	0.004104	0.999907	6.037×10^{-4}
B joint closure	9.306×10^{-5}	1.506×10^{-4}	1.3510	2.6171	4.6661	0.004104	0.999907	6.025×10^{-4}
C ideal balanced	9.301×10^{-5}	0	0.0000	2.6170	4.6622	0.004104	0.999907	1.509×10^{-4}

The differential-only solution reduces both target displacements, so Eq. (S97) also places B_{common} below the chosen 10^{-3} model coordinate. Adding the common-motion penalty changes it only from 1.509×10^{-4} to 1.506×10^{-4} and does not materially reduce the 1.3510-rad local-phase RMS. The common-motion burden is therefore reduced below this coordinate for the representative pair and bounded basis; the local phase remains a separate calibration burden. If a future pair or control basis exceeds the same common-motion coordinate, the analysis reports that burden separately from D_{ij}.

For a subsequent operation that is sensitive to absolute motion, we report

$$B_{\mathrm{next}}^{\max} = \max_{z_i, z_j = \pm 1} \sum_m (2\bar{n}_m + 1)|\beta_m + z_i\alpha_{im} + z_j\alpha_{jm}|^2. \tag{S98}$$

This is a model-level motional-state burden, not a simulated error of a specific later gate. The same-gate conditional-Ramsey contrast depends on the arm difference and therefore cancels the common β_m contribution, as derived in Section S4.

The waveform objective, summary table, passband definitions, and validation range are given below. Additional comparisons of unshaped and optimized envelopes, motional closure, and passband response were generated in the authors' working source-data tree; Fig. 3 of the main text summarizes these results.

S15.2 Three-class waveform synthesis

The expanded synthesis compares three control classes under identical hard constraints. Class A assigns a piecewise-constant scalar amplitude to each active target window, in addition to the fixed rise/fall edge. Class B multiplies each window by a positive sampled two-harmonic Fourier envelope. Class C adds programmable boundary phases to the scalar-amplitude schedule while bounding every adjacent phase increment by 0.8 rad. All classes use the continuous boundary-phase rule as the operating mode. Reset, scrambled, and gap-frozen rules are evaluated only as controls.

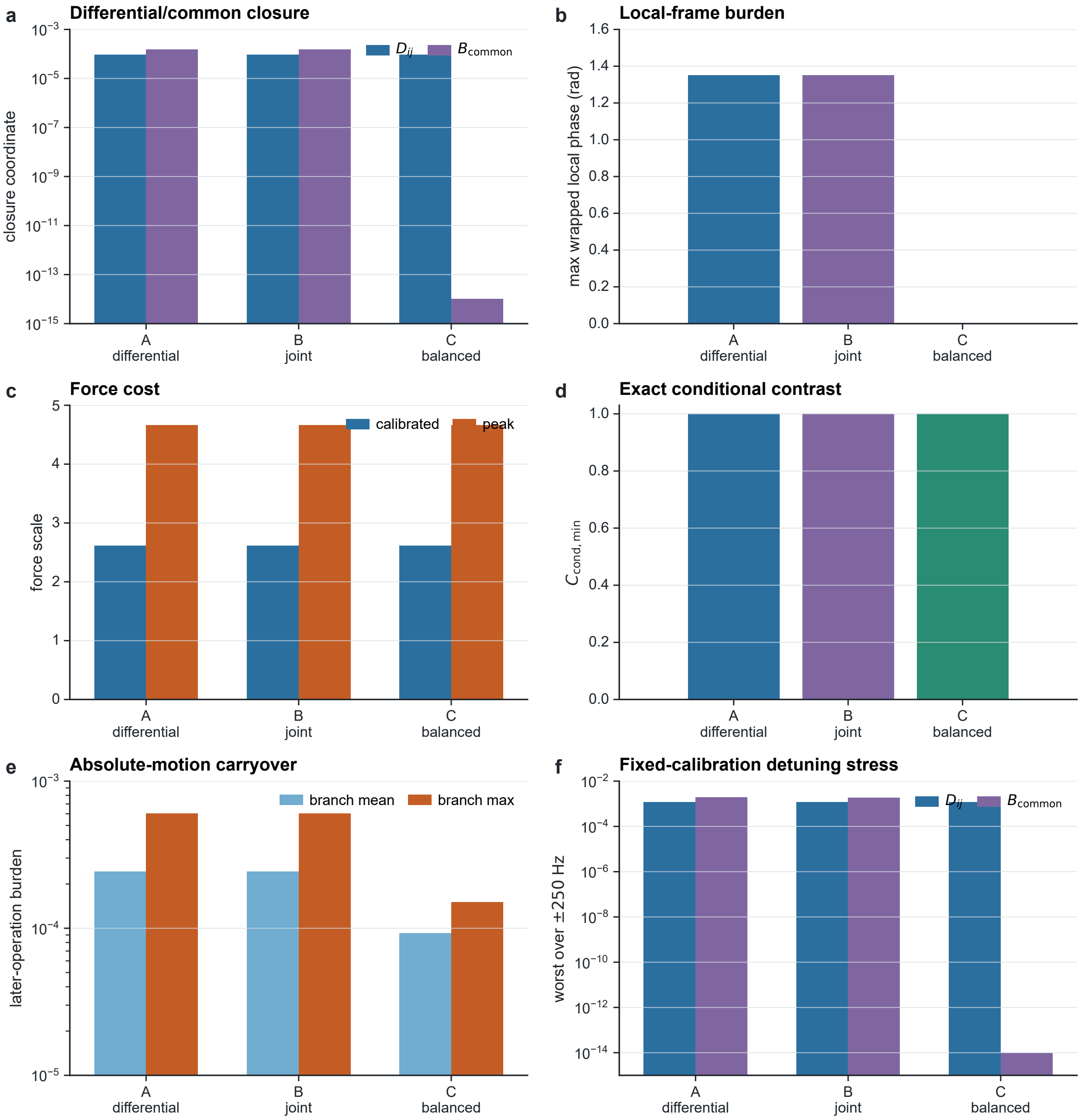

Supplementary Figure S8: Common/differential closure trade-off. The panels compare differential and common closure, wrapped local phase, force cost, exact conditional-Ramsey contrast, the absolute-motion coordinate for a later operation, and fixed-calibration ±250 Hz detuning stress.

For every optimizer evaluation, $s_i(t)s_j(t) = 0$, target-to-target leakage is zero, and the force vanishes throughout switching gaps. A separate spectator-only leakage matrix is used to calculate spectator ZZ without introducing residual simultaneous target forcing. Candidates violating the target-window, dark-gap, or illumination constraints are excluded from the admissible control set.

The model-level optimization objective is

$$\mathcal{J} = 40\epsilon_\Phi^2 + D_{ij} + 20Z_{\rm spec}^2 + 10^{-3}P_{\rm int} + 10^{-3}P_{\rm peak} + 8R_\delta + 8R_\phi, \tag{S99}$$

where $\epsilon_\Phi = |\,{\rm wrap}_{2\pi}(\Phi_{ij} - \Phi_{\rm target})|$, using the convention in Eq. (S81), $D_{ij} = \sum_m (2\bar{n}_m + 1)(|\alpha_{im}|^2 + |\alpha_{jm}|^2)$, $Z_{\rm spec}$ is the maximum non-target pair phase under the specified spectator-only leakage diagnostic, $P_{\rm int}$ and $P_{\rm peak}$ penalize integrated squared and peak force, and R_δ and R_ϕ average detuning and window-phase-noise perturbations. This objective is a model-design functional rather than a physical error rate.

Supplementary Table S17: Three-class waveform-synthesis readouts. All entries are simulation estimates.

Case	wrapped error	D_{ij}	spectator ZZ	force scale	peak scale
unshaped	0	1.2217×10^{-1}	0.005420	3.7704	3.7704
A: piecewise	0	1.5320×10^{-4}	0.005370	2.8455	5.4379
B: Fourier	0	9.1716×10^{-5}	0.005373	2.8399	5.8074
C: phase programmed	0	1.2004×10^{-4}	0.004130	2.4685	4.7541

The integrated force-area coordinates for A, B, and C are 618.92, 618.09, and 539.26 scale-microseconds, compared with 687.72 for the unshaped reference. The direct ordered double integral gives -0.785398 rad for every optimized class and agrees with the Magnus recurrence to better than 10^{-8} rad while the target overlap and hidden gap force remain exactly zero on the numerical grid. The displayed class-B solution has a displacement coordinate 7.51×10^{-4} times the unshaped value, but the multistart analysis below shows that this single ratio is not a class-wide robustness statement.

The final robustness output scans residual detuning over ± 500 Hz, window-phase noise up to 0.03 rad rms, and switching jitter up to 0.2 microseconds, and separately evaluates continuous, reset, scrambled, and gap-frozen phase rules. These scans hold the optimized nominal force calibration fixed. They quantify model sensitivity and do not establish experimental performance.

S15.3 Multistart, objective-weight, and formulation sensitivity

The three representative solutions above illustrate feasible endpoints; optimizer sensitivity is assessed separately through multistart and objective-weight analyses. We therefore run 32 independent Latin-hypercube starts for every waveform class using the same weighted objective, and separately run 32 starts with a lexicographic constrained formulation that minimizes $D_{ij} + B_{\rm common}$ only after satisfying the specified phase, spectator, force, phase-increment, zero-overlap, zero-dark-gap-force, approximation-screening, and control-resource constraints. The approximation and control conditions are evaluated independently. The weighted objective is also repeated while scaling each of its phase, closure, spectator, force, and robustness groups by 0.1, 0.3, 1, 3, and 10, one group at a time.

Supplementary Table S18: Waveform-optimization feasible-endpoint distributions. Feasible is the fraction of starts whose final point satisfies every declared physical constraint, not a hardware yield or a guarantee of step-tolerance termination. D_{10}, D_{50}, and D_{90} are feasible-endpoint quantiles.

Class	feasible (%)	$D_{\rm best}$	D_{10}	D_{50}	D_{90}	improvement 10–50–90%	constrained feasible (%)	step term. (%)
Piecewise	93.8	5.296×10^{-6}	5.408×10^{-5}	1.319×10^{-4}	5.316×10^{-4}	229.8–927.0–2267.7	100.0	18.8
Fourier	84.4	2.395×10^{-5}	4.719×10^{-5}	1.533×10^{-4}	5.965×10^{-4}	209.9–796.9–2612.3	100.0	0.0
Phase programmed	75.0	1.235×10^{-4}	2.044×10^{-4}	6.760×10^{-4}	1.901×10^{-3}	65.2–180.8–597.6	100.0	0.0

The weighted-sum feasibility fractions are 93.8%, 84.4%, and 75.0%, whereas the independent constrained formulation finds feasible endpoints for 100.0%, 100.0%, and 100.0% of starts. Only

18.8%, 0.0%, and 0.0% of the baseline-budget weighted searches reach the step-tolerance termination state. The remaining constraint-satisfying endpoints are therefore feasible designs found within the declared numerical budget, not local optima. The phase-programmed class is the most initialization-sensitive of the three, and force-weight rescaling produces its largest closure degradation. In the authors' working tree, the full row-level starts, endpoints, constraints, iteration counts, runtimes, weight scans, and failure flags are stored as `data/optimizer_multistart_results.csv`, `data/objective_weight_sensitivity.csv`, and `data/constrained_optimizer_results.csv`; these files are available upon reasonable request.

To separate feasibility from numerical termination, the same 32 starts are followed for one, two, and four times the baseline iteration budget. The derivative-free search does not provide a gradient norm or a constraint-tolerance stopping rule, so constraint satisfaction, optimizer success, step termination, and endpoint stability are reported independently. Endpoint stability compares the two- and four-times endpoints using fixed numerical comparison thresholds and is not itself an optimizer stopping condition.

Supplementary Table S19: Four-times-budget convergence and endpoint classification. Objective and endpoint stability compare the two- and four-times endpoints. "Conv." counts feasible endpoints that also reached the normalized step tolerance; "budget" counts feasible designs that exhausted the numerical budget.

Formulation	class	feasible (%)	step term. (%)	objective stable (%)	endpoint stable (%)	conv.	budget	infeasible	numerical failure
weighted	piecewise	93.8	96.9	84.4	81.2	29	1	2	0
weighted	Fourier	90.6	96.9	65.6	46.9	28	1	3	0
weighted	phase-programmed	78.1	96.9	59.4	50.0	24	1	7	0
constrained	piecewise	100.0	100.0	93.8	93.8	32	0	0	0
constrained	Fourier	100.0	96.9	46.9	40.6	31	1	0	0
constrained	phase-programmed	100.0	100.0	59.4	59.4	32	0	0	0

At four-times budget, weighted piecewise endpoints are 81.2% stable between the two final budgets, compared with 46.9% for Fourier and 50.0% for phase-programmed control. The corresponding constrained values are 93.8%, 40.6%, and 59.4%. These results motivate the use of piecewise control as a representative budget-stable feasible design. The Fourier class reaches a lower median D_{ij} but shows weaker endpoint stability. Endpoint stability is reported as a descriptive comparison rather than a prespecified convergence test.

S15.4 Passband-aware closure and drift-moment diagnostics

Nominal closure constrains the zeroth time moment of the force but does not constrain its higher moments. To keep the displacement convention explicit, denote the real amplitude in Eq. (S13) by $G^{(F)}_{qm}(t) \equiv G_{qm}(t)$ and define the displacement-kernel prefactor

$$\mathcal{K}_{qm}(t) = -\frac{i}{2}G^{(F)}_{qm}(t), \qquad \Delta_m = 2\pi(\nu_m - \mu), \qquad \phi_q(t) = -\varphi_q(t). \tag{S100}$$

For the nominal compensated drive, these definitions make $\mathcal{K}_{qm}(t)e^{i[\Delta_m t+\phi_q(t)]} = -iF^*_{qm}(t)$, exactly reproducing the displacement convention $\alpha_{qm} = -i\int F^*_{qm}dt$ used above, including the factor of 1/2 and the complex conjugation. A positive δ below denotes an angular *mode-frequency* drift, so that the mode-minus-drive detuning becomes $\Delta_m + \delta$. The drift-dependent displacement is therefore

$$\alpha_{qm}(\delta) = \int_0^T dt\, \mathcal{K}_{qm}(t)e^{i[(\Delta_m+\delta)t+\phi_q(t)]}, \tag{S101}$$

and its derivatives are

$$\frac{\partial \alpha_{qm}}{\partial \delta} = i\int_0^T dt\, t\mathcal{K}_{qm}(t)e^{i[(\Delta_m+\delta)t+\phi_q(t)]}, \tag{S102}$$

$$\frac{\partial^2 \alpha_{qm}}{\partial \delta^2} = -\int_0^T dt\, t^2\mathcal{K}_{qm}(t)e^{i[(\Delta_m+\delta)t+\phi_q(t)]}. \tag{S103}$$

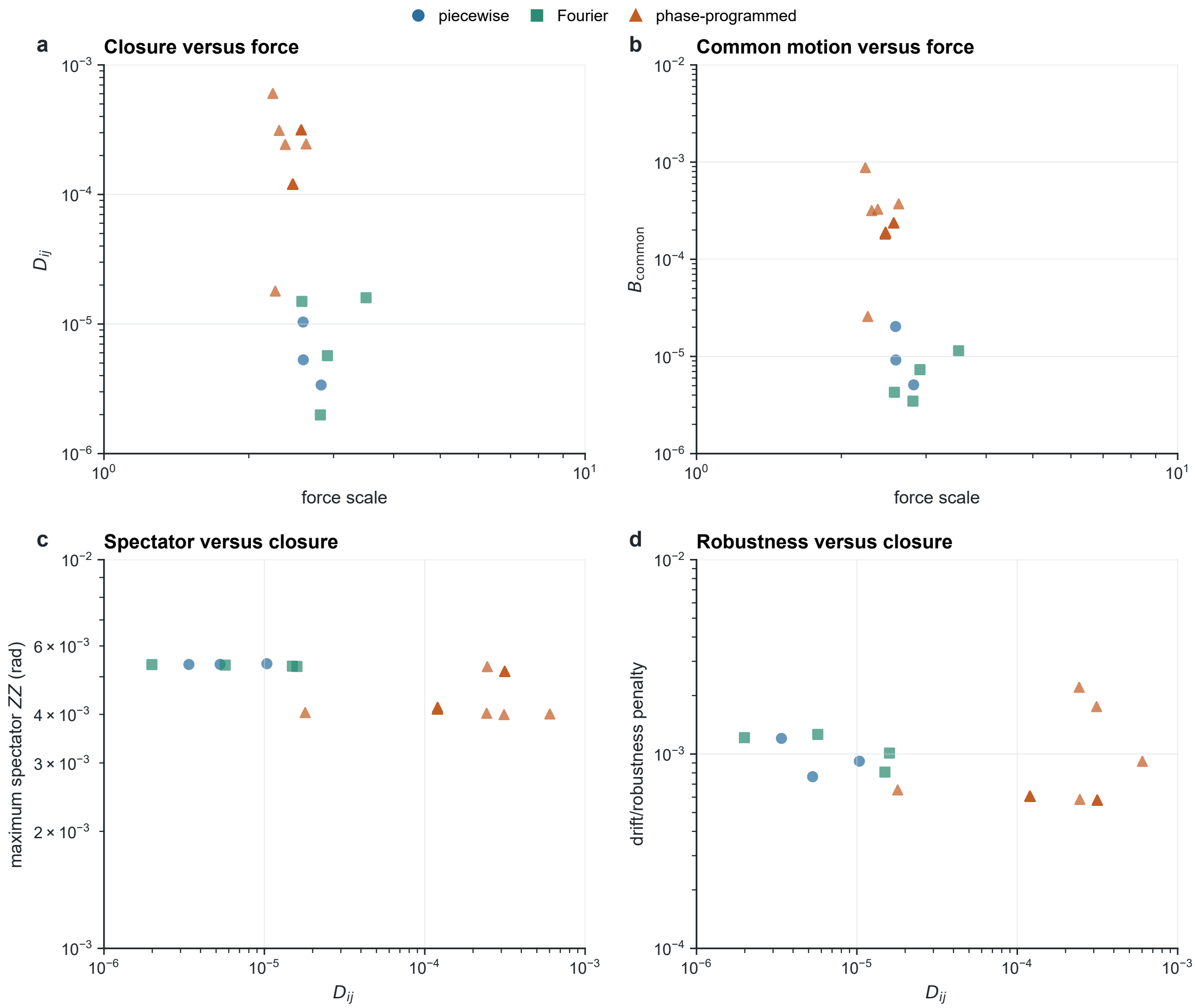

Supplementary Figure S9: Nondominated feasible-design comparison. The 46 feasible endpoints expose D_{ij}–force, B_{common}–force, spectator–D_{ij}, and drift–closure trade-offs. Nondominance is defined only within the sampled feasible-design set.

For the ordinary-frequency drift δ_f used in the CSV, $\delta = 2\pi\delta_f$, so the first and second derivatives acquire factors 2π and $(2\pi)^2$, respectively. The thermal displacement curvature is

$$\frac{d^2D}{d\delta_f^2} = 2\sum_{q\in\{i,j\},m}(2\bar{n}_m+1)\left(\left|\frac{d\alpha_{qm}}{d\delta_f}\right|^2 + \mathrm{Re}\left[\alpha_{qm}^*\frac{d^2\alpha_{qm}}{d\delta_f^2}\right]\right). \tag{S104}$$

Consequently, $\alpha_{qm}(0) \simeq 0$ alone is insufficient: the first-moment term can make D rise quadratically immediately outside the nominal calibration point.

The passband-aware objective adds five direct terms to the nominal phase/force/spectator functional: $D(0)$; $|D''(0)|$; the sampled maximum $D(\delta_f)$ over $|\delta_f| \le 100$ Hz; an optional lower-weight stress maximum over $|\delta_f| \le 500$ Hz; and the worst wrapped target-phase error over the same bands. All mode frequencies receive the same shift, the nominal force scale is held fixed, target windows remain disjoint, and no force is inserted in dark gaps. The analytic curvature agrees with a ± 10 Hz central difference to relative error 8.3×10^{-6} for the passband-aware solution.

Supplementary Table S20: Baseline and passband-aware waveform diagnostics. All entries are model-level drift-robustness estimates, not measured tolerances.

Waveform	$D(0)$	$D''(0)$ (Hz^{-2})	$\max_{100} D$	$\max_{500} D$	$\max_{100}\lvert\Delta\Phi\rvert$ (rad)	force scale
baseline optimized Fourier	9.17×10^{-5}	4.38×10^{-8}	3.48×10^{-4}	5.57×10^{-3}	0.00371	2.840
passband-aware Fourier/phase	5.85×10^{-6}	3.40×10^{-8}	1.81×10^{-4}	4.36×10^{-3}	0.00429	2.546

The passband-aware solution lowers the ±100 Hz worst-case displacement by 48.0% and the curvature magnitude by 22.5%. This improvement is accompanied by a modest increase in worst-case phase error within the design band, from 0.00371 to 0.00429 rad, and a peak-force change from 5.807 to 5.923 in the model scale. The maximum spectator ZZ decreases from 0.00537 to 0.00431 rad. Thus the broader closure window is accompanied by changes in phase error, peak force, and spectator coupling and should be interpreted as a control trade-off.

The machine-readable schedules contain the 72 optimized-window records and the baseline/passband comparison programs. The drift-moment file contains mode-resolved α, $d\alpha/d\delta_f$, $d^2\alpha/d\delta_f^2$, aggregate curvature checks, and 10 Hz-spaced drift curves. Optimization of one representative pair does not establish closure or drift robustness for every physical-chain pair.

S16. All-Pair Analysis for Physical Ion Chains

S16.1 Fixed-schedule all-pair atlas

For every $i < j$ pair, four boundary-phase offsets are tested and the target-sign candidate with the largest unit-force phase is selected before scalar force calibration. All synthesis rows use zero intended target overlap. The scan then records the force scale F_{ij}, the target thermal-displacement diagnostic

$$D_{ij} = \sum_m (2\bar{n}_m+1)(|\alpha_{im}|^2 + |\alpha_{jm}|^2), \tag{S105}$$

the maximum target–spectator phase, the dominant mode and its absolute phase fraction f_{ij}^{dom}, and a central-difference common-mode detuning response evaluated at ±250 Hz. The mode-drift score is

$$C_{ij}^{\mathrm{drift}} = \frac{|\partial\Phi_{ij}/\partial\delta_f|}{0.05\ \mathrm{rad\,kHz^{-1}}}\left(0.5 + f_{ij}^{\mathrm{dom}}\right). \tag{S106}$$

Here δ_f is the common ordinary-frequency mode drift, expressed in kilohertz for the derivative in this score; it is the same coordinate used in Section S15.4. The force, closure, spectator, and drift boundaries are respectively 25, 0.25, 0.02 rad, and $C_{ij}^{\mathrm{drift}} = 1$. They are declared coordinates for partitioning this reduced-model atlas, not universal tolerances or apparatus specifications. For the same zero-leakage waveform, the idealized single-projector model additionally gives the common-motion coordinate

$$B_{\text{common}} = \sum_m (2\bar{n}_m + 1)|\beta_m|^2. \tag{S107}$$

This coordinate is calculated independently rather than inferred from D_{ij}; the 0.006 scalar leakage is introduced only for the spectator-ZZ diagnostic.

The baseline A–E burden labels are mutually exclusive. A requires all four normalized burdens to be at most one. B denotes a target-sign-controllable pair above the force boundary. Among force-feasible non-A pairs, D takes priority when the spectator boundary is exceeded, E then identifies a drift-score exceedance, and C labels the remaining closure exceedance. This B–D–E–C rule assigns one primary control-burden label but necessarily hides other simultaneous exceedances; the output therefore stores every secondary flag, and the main analysis uses continuous burdens and Pareto rank. Reduced-Hamiltonian approximation screening is stored separately and never replaces an A–E label.

Supplementary Table S21: Auxiliary all-pair control-burden counts (simulation estimate). A–E labels classify declared control coordinates only. Reduced-Hamiltonian approximation screening is reported separately; these fractions are not hardware success probabilities.

N	pairs	A	B	C	D	E
5	10	0	0	5	2	3
10	45	0	0	0	11	34
20	190	1	144	19	2	24
30	435	12	384	6	6	27
All	680	13	528	30	21	88

Supplementary Table S22: Continuous all-pair burden summary. Entries are $p_{10}/p_{50}/p_{90}$ over all pairs at each N. B_{common} uses the idealized single-projector limit at zero leakage; spectator ZZ uses the 0.006 scalar-leakage diagnostic.

N	pairs	approx. pass	force $p_{10}/p_{50}/p_{90}$	D_{ij} $p_{10}/p_{50}/p_{90}$	B_{common} $p_{10}/p_{50}/p_{90}$	spectator ZZ p_{50} (rad)	drift score p_{50}
5	10	10	2.88/3.52/6.66	2.35/2.74/3.9	2.5/3.96/4.51	0.00647	1.48
10	45	13	5.4/9.92/17.2	6.23/21.2/45.5	4.57/26.5/59	0.00854	19.7
20	190	127	12/48.4/112	0.639/7.98/52.1	0.74/7.12/50.5	0.0357	5.04
30	435	0	19.5/145/422	0.513/5.81/95.8	0.502/5.34/95.4	0.157	2.18

Supplementary Table S23: Reduced-Hamiltonian approximation-screening counts. Pass, warning, and outside-tested-range refer only to the evaluated motional indicators. Optical adiabatic-elimination validity is unavailable without complete atomic inputs; control burdens are classified independently.

N	approximation pass	warning	outside tested range
5	10	0	0
10	13	22	10
20	127	36	27
30	0	302	133

Supplementary Table S24: Representative pair from each all-pair design regime (simulation estimate). Each row is nearest the regime median in log burden-score space rather than a best- or worst-case selection. Ion indices in the table are one-based.

Regime	N	pair	force scale	D_{ij}	max spectator ZZ (rad)	m_{dom} (f_{dom})	$\lvert\partial\Phi/\partial\delta_f\rvert$ (rad kHz^{-1})
A	30	$(18, 19)$	8.97	0.146	0.00399	0 (0.59)	0.027
B	20	$(15, 20)$	68.3	12.5	0.105	15 (0.40)	0.226
C	20	$(7, 12)$	8.1	0.438	0.00435	1 (0.60)	0.0264
D	10	$(7, 10)$	16.8	16.8	0.0317	6 (0.58)	0.472
E	20	$(5, 13)$	18.5	2.04	0.00844	5 (0.32)	0.219

All 680 pairs are algebraically target-sign reachable after the four-offset search within the reduced solver, and all 680 expose both phase signs in that menu. This is a phase-selection property of the tested offsets, not an approximation-validity or scalability result. The motional approximation screening finds 150 pass, 360 warning, and 170 outside-tested-range rows; optical validity is unavailable for all 680 rows. Independently, 27 rows satisfy the declared force, differential-closure, and spectator coordinates, while one row lies in both that subset and the motional approximation-pass subset. The all-pair atlas is a design map, not a scalability claim. Baseline scalar leakage is applied only after ideal zero-overlap synthesis; the output separates target-phase perturbation and target–spectator ZZ from the mechanism-defining phase.

S16.2 Reduced-Hamiltonian approximation screening and control-resource burden

For each main-text representative, fixed-schedule pair, pair-specific optimization row, and idealized single-projector apparatus-interface row, the authors' reproducibility workflow records

$$\epsilon_{\mathrm{LD}} = \max_{j\in\{i,j\},m} |\eta_{jm}|\sqrt{2\bar{n}_m + 1}, \qquad \epsilon_{\mathrm{LD}}^{(2)} = \epsilon_{\mathrm{LD}}^2/2, \tag{S108}$$

as the static thermal coordinate. To include coherent motion accumulated during the pulse, the same integration grid is used to retain the partial displacements

$$\alpha_{qm}(t) = -i\int_0^t g_{z,qm}(t')e^{i\omega_m t'}dt', \qquad \beta_m(t) = -i\int_0^t G_{0m}(t')e^{i\omega_m t'}dt'. \tag{S109}$$

For each target computational-basis branch $\mathbf{z} = (z_i, z_j)$, with all driven spectators in the declared $Z = -1$ reference state, the branch trajectory is

$$A_m(\mathbf{z}, t) = \beta_m(t) + \sum_q z_q\alpha_{qm}(t). \tag{S110}$$

The conservative dynamic screening coordinate is

$$\epsilon_{\mathrm{LD,dyn}} = \max_{j,m,t,\mathbf{z}} |\eta_{jm}|\sqrt{2\bar{n}_m + 1 + 4|A_m(\mathbf{z}, t)|^2}. \tag{S111}$$

This is explicitly a conservative magnitude bound. The phase-resolved position-quadrature second moment provides the independent cross-check

$$\epsilon_{\mathrm{LD,quad}} = \max_{j,m,t,\mathbf{z}} |\eta_{jm}|\sqrt{2\bar{n}_m + 1 + 4\left[\mathrm{Re}(A_m(\mathbf{z}, t)e^{-i\omega_m t})\right]^2}. \tag{S112}$$

For a displaced thermal state the centered quadrature variance remains $2\bar{n}_m + 1$; the coherent displacement contributes the phase-dependent squared mean in Eq. (S112). Therefore $\epsilon_{\mathrm{LD,quad}} \leq \epsilon_{\mathrm{LD,dyn}}$, while Eq. (S111) is used for classification. The peak retained near-resonant force divided by the minimum discarded sum-frequency separation, the directly integrated discarded counter-rotating displacement divided by the retained-force displacement coordinate, and the 99% spectral-energy bandwidth of the programmed complex envelope divided by that same fast separation supply the other approximation coordinates. The peak force divided by the nearest sideband detuning and minimum mode spacing is instead a control-resource and multimode-selectivity diagnostic; it never changes the approximation-screening label.

The declared warning/outside-tested-range boundaries are 0.15/0.25 for both the static and conservative dynamic Lamb–Dicke coordinates, 0.02/0.10 for retained force over sum frequency, 0.20/0.40 for envelope bandwidth over sum frequency, and 0.02/0.05 for the directly integrated counter-rotating displacement ratio. These are numerical screening coordinates rather than literature-calibrated apparatus tolerances. Dynamic trajectories are evaluated for 957 publication and stress rows; four representative points are recomputed with $dt/2$, for which the largest relative change is 3.56×10^{-3}. Three direct points additionally use the full real-force solver at dt, $dt/2$, and $dt/4$ and are compared with the complex-RWA recurrence: the optimized five-ion representative, a 30-ion point nearest the force cap from below, and the maximum-force atlas row. Time-grid and solver-agreement tests are numerical verification results rather than classification inputs. Separate row-level CSV tables report approximation screening, dynamic trajectories, and control-resource burdens.

S16.3 Threshold sensitivity and priority-rule analysis

The A–E atlas uses nominal boundaries $F = 25$, $D_{ij} = 0.25$, $Z_{\mathrm{spec}} = 0.02$ rad, and drift score = 1. We scanned uniform scaling factors $0.5, 0.75, 1.0, 1.5, 2.0$ and repeated one-at-a-time scans for each boundary. For every pair, the analysis records the primary label in every threshold scenario, label stability, transition matrices, regime-count curves, secondary limitations hidden by the B–D–E–C priority rule, continuous burden scores, and a four-dimensional Pareto rank in force, displacement, spectator-ZZ, and drift coordinates. The A–E label identifies the primary burden under the specified priority rule; it is neither a complete diagnosis nor a hardware-success probability.

For the baseline A–E burden classifier, the mean nominal-label stability fraction is 0.956, and 97.8% of pairs retain their nominal burden label in at least 75% of the tested threshold scenarios. This sensitivity calculation concerns control-burden labels only and does not alter reduced-Hamiltonian approximation screening. However, 623 of 680 pairs have at least one secondary limitation hidden by the priority rule. The hidden-secondary counts are 0 force, 623 closure, 474 spectator, and 445 drift exceedances; one pair can contribute to several columns. Secondary flags and continuous scores should therefore be used whenever a pair is selected for detailed design.

Figure 6(e,f) of the main text shows fixed-schedule force versus ion-pair separation and the corresponding chain-length statistics, with approximation categories reported separately. The thresholded A–E map is included below as an auxiliary control-burden view rather than the primary scaling result.

S16.4 Pair-specific and mode-adapted optimization study

The all-pair atlas uses one common schedule and therefore does not give the best control found for each pair. We examine a deliberately stratified design sample of 81 pairs selected across $N = 5, 10, 20, 30$, pair separation, and the initial A–E burden labels. It is not a random sample and its fractions are not hardware yields. The Hamiltonian-level study has three layers. L1 recomputes the fixed common schedule for each physical-chain pair. L2 applies a deterministic bounded coordinate search to the six-parameter amplitude/boundary-phase waveform of Section S15. L3 first searches physical control coordinates and then repeats the waveform search. Every objective evaluation regenerates the force and evaluates the Magnus recurrence; no output in this subsection is obtained by multiplying an atlas value by an assumed improvement factor.

For L2 the objective is

$$\mathcal{J}_{\mathrm{pair}} = D_{ij} + B_{\mathrm{common}} + 2 \times 10^{-5} \left(\frac{F_{\mathrm{peak}}}{8} \right)^2 + 10^{-8} \mathcal{I}_2 + 0.002 \, [\max(0, F - 25)]^2, \tag{S113}$$

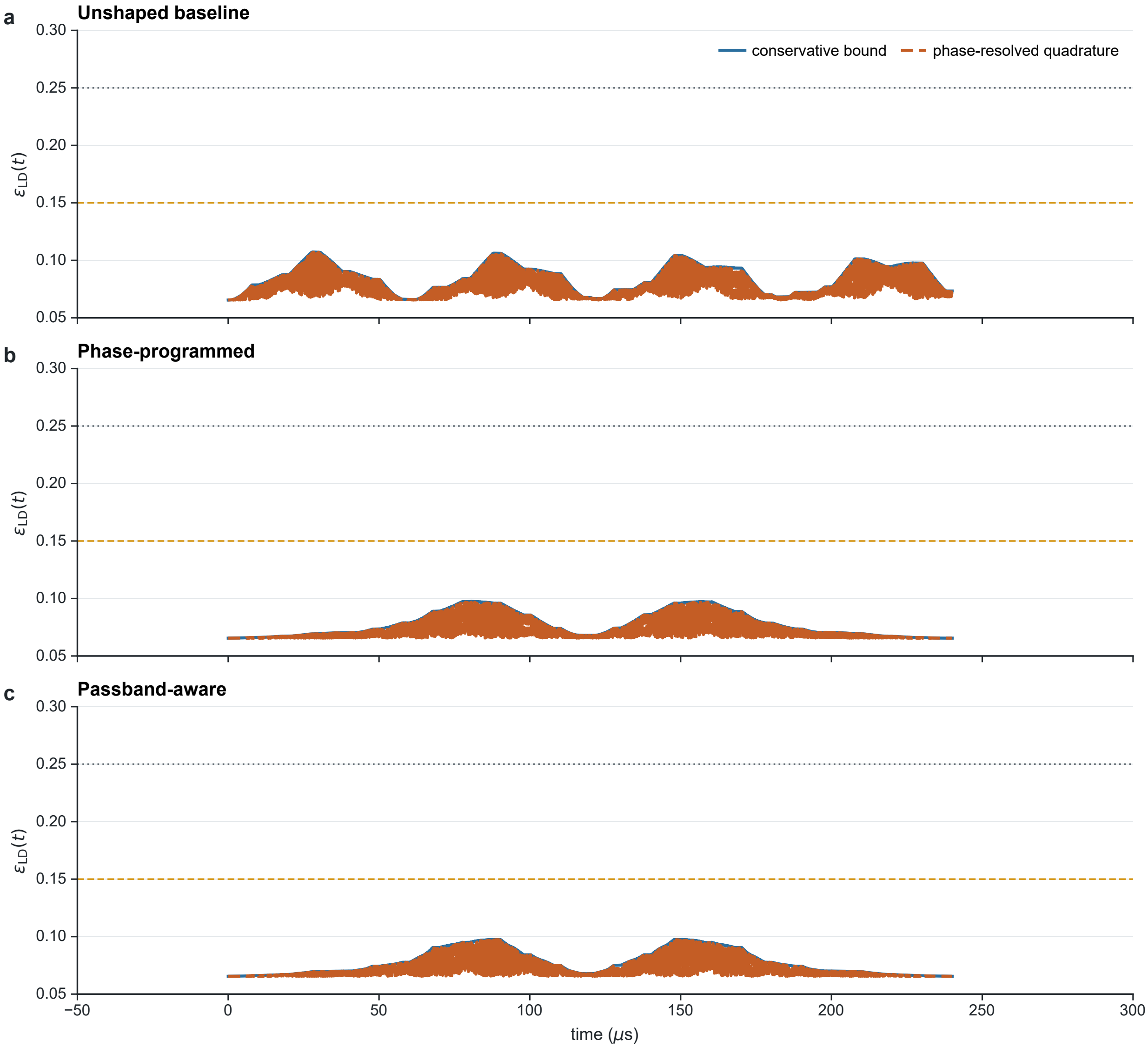

Supplementary Figure S10: Time-resolved Lamb–Dicke coordinates. The traces show the conservative bound in Eq. (S111) and the phase-resolved quadrature coordinate in Eq. (S112) for representative unshaped, phase-programmed, and passband-aware schedules. Horizontal lines mark the declared warning and outside-tested-range screening coordinates. The conservative bound retains the data even when a trajectory leaves the tested range; it is not a gate-error or fidelity estimate. The seeded scrambled aggregate is reported separately in the row-level source data because its publication coordinate is the maximum over the declared ensemble rather than a single trajectory.

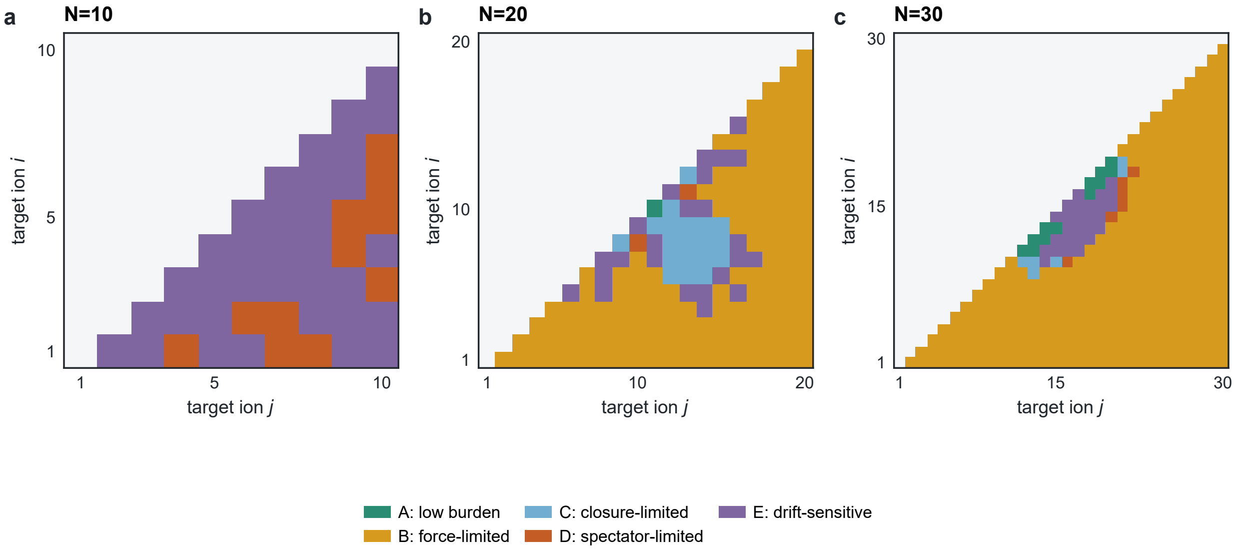

Supplementary Figure S11: Auxiliary A–E control-burden maps (simulation estimate). The upper-triangular maps use one-based ion indices and show Regimes A–E for $N = 10$, 20, and 30. Each label supplies one threshold-dependent primary control burden and does not replace the continuous coordinates, secondary flags, or independent reduced-Hamiltonian approximation screening.

where $\mathcal{I}_2$ is the integrated squared-force coordinate. The signed pair phase is recalibrated to $-\pi/4$ at every objective call. L3 evaluates target-mode candidates $m \in \{0, m_{\rm dom}, m_{\rm dom} \pm 1\}$, beat-note choices $\mu = \nu_m + \{8, 16, 24\}$ kHz, gaps $\{1, 2, 4\}$ microseconds, windows $\{6, 8, 10\}$ microseconds, cycle counts $\{8, 12, 16\}$, and relative boundary phases $\{0, \pi/2, \pi, 3\pi/2\}$, followed by another bounded waveform search. The target-mode index is therefore the mode around which μ is placed, not a modification of the physical eigenmode spectrum.

All three levels enforce zero target-window overlap, zero hidden dark-gap force, no simultaneous target illumination, and adjacent programmed phase increments no larger than 0.8 rad. The common displacement is evaluated from the idealized single-projector relation $\beta_m = \alpha_{im} + \alpha_{jm}$. The worst-direction conditional contrast is

$$C_{\rm cond,min} = \min_{q\in\{i,j\}} \exp\left[-2\sum_m (2\bar{n}_m + 1)|\alpha_{qm}|^2\right]. \tag{S114}$$

Spectator ZZ is computed only after optimization by restoring the declared 0.006 scalar leakage diagnostic. Common-mode drift robustness is the central response to ± 100 Hz shifts of every motional frequency at fixed force calibration.

Supplementary Table S25: Approximation screening of the deliberately stratified pair-specific sample. Optical adiabatic-elimination validity is a separate, overlapping unavailable flag because apparatus atomic inputs are absent. Counts are design-sample diagnostics, not yields.

Level	N	pass	warning	outside tested range	optical unavailable
L1	5	10	0	0	10
L1	10	8	6	6	20
L1	20	18	0	0	18
L1	30	0	28	5	33
L1	all	36	34	11	81
L2	5	10	0	0	10
L2	10	8	12	0	20
L2	20	18	0	0	18
L2	30	0	28	5	33
L2	all	36	40	5	81
L3	5	10	0	0	10
L3	10	20	0	0	20
L3	20	18	0	0	18
L3	30	6	27	0	33
L3	all	54	27	0	81

Supplementary Table S26: Pass-subset and all-sample medians. The pass cohort changes from 36 at L1/L2 to 54 at L3; the all column contains all 81 deliberately selected pairs.

Level	quantity	median over pass	median over all
L1	D_{ij}	2.4002	1.6916
L1	B_{common}	2.8746	2.4836
L1	$C_{\mathrm{cond,min}}$	0.0419	0.1729
L1	force scale	6.738	12.223
L1	duration (μs)	240.0	240.0
L1	drift response (rad kHz^{-1})	0.0857	0.0762
L1	dynamic ϵ_{LD}	0.0729	0.0787
L2	D_{ij}	1.2048	0.9411
L2	B_{common}	1.4781	0.5616
L2	$C_{\mathrm{cond,min}}$	0.2616	0.3194
L2	force scale	5.309	9.065
L2	duration (μs)	240.0	240.0
L2	drift response (rad kHz^{-1})	0.1492	0.0630
L2	dynamic ϵ_{LD}	0.0680	0.0689
L3	D_{ij}	0.1230	0.0633
L3	B_{common}	0.1020	0.0531
L3	$C_{\mathrm{cond,min}}$	0.8662	0.9215
L3	force scale	4.256	5.146
L3	duration (μs)	264.0	320.0
L3	drift response (rad kHz^{-1})	0.0775	0.0435
L3	dynamic ϵ_{LD}	0.0525	0.0530

The level counts are 36/34/11 pass/warning/outside at L1, 36/40/5 at L2, and 54/27/0 at L3. Thus L3 moves 18 L2 warning/outside rows into the pass category, but 27 rows remain warnings. For all 81 pairs, the L3 closure and contrast medians improve relative to L1 while the median duration increases. Within the level-specific pass subsets, D_{ij} is 2.4002 at L1 and 0.1230 at L3, whereas the corresponding all-sample medians are 1.6916 and 0.0633. These two summaries must be read together because the pass cohort changes with control level. Average two-qubit channel fidelity is not stored at pair-row resolution and is not inferred from $C_{\mathrm{cond,min}}$. In the authors' working tree, the complete strata by initial burden, pair separation, and dynamic Lamb–Dicke class are stored as `data/pair_specific_validity_stratified.csv` and are available upon reasonable request.

The authors' working reproducibility tree contains the complete 3×81-row output, convergence state, selected μ, mode, timing, boundary phase, waveform parameters, hard-constraint checks, validity strata, same-pair transitions, and dedicated completeness checks. Its internal README records file-level provenance and reproduction commands. Source data and code are available from the corresponding authors upon reasonable request, as stated in Section S18.

S17. Robustness to Control Imperfections

S17.1 Control-parameter grids and reduced-model response

The robustness analysis holds the optimized nominal force calibration fixed and scans fifteen control-parameter axes, including linear and rise/fall-transient AOD chirps, common and mode-dependent random drift, seeded inter-window boundary-phase noise, and a scrambled-boundary control. Deterministic axes are evaluated once per grid point, whereas stochastic axes use 512 fixed seeds per point. Results from the reduced-force and idealized single-projector models are reported separately and represent simulated sensitivity rather than experimental performance.

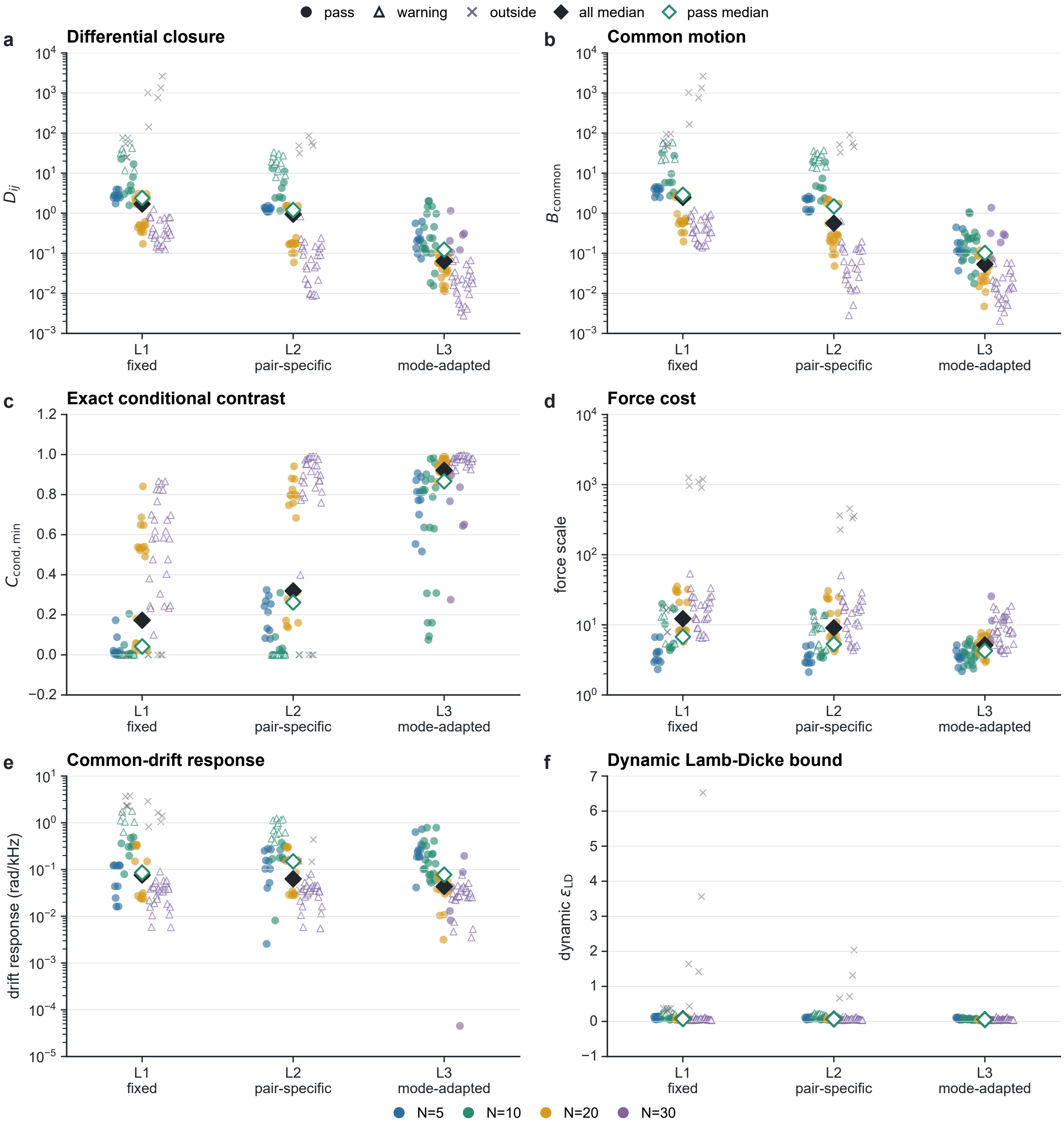

Supplementary Figure S12: Fixed, pair-specific, and mode-adapted controls. Each point is recomputed from the physical-chain Hamiltonian. Color identifies chain size; filled circles, open triangles, and crosses identify approximation pass, warning, and outside-tested-range rows. Black and green diamonds show all-sample and pass-subset medians, respectively. The closure, worst-direction conditional contrast $C_{\mathrm{cond,min}}$, force, duration, drift, and dynamic Lamb–Dicke coordinates expose both improvement and selection effects; they are not measured fidelities or hardware tolerances.

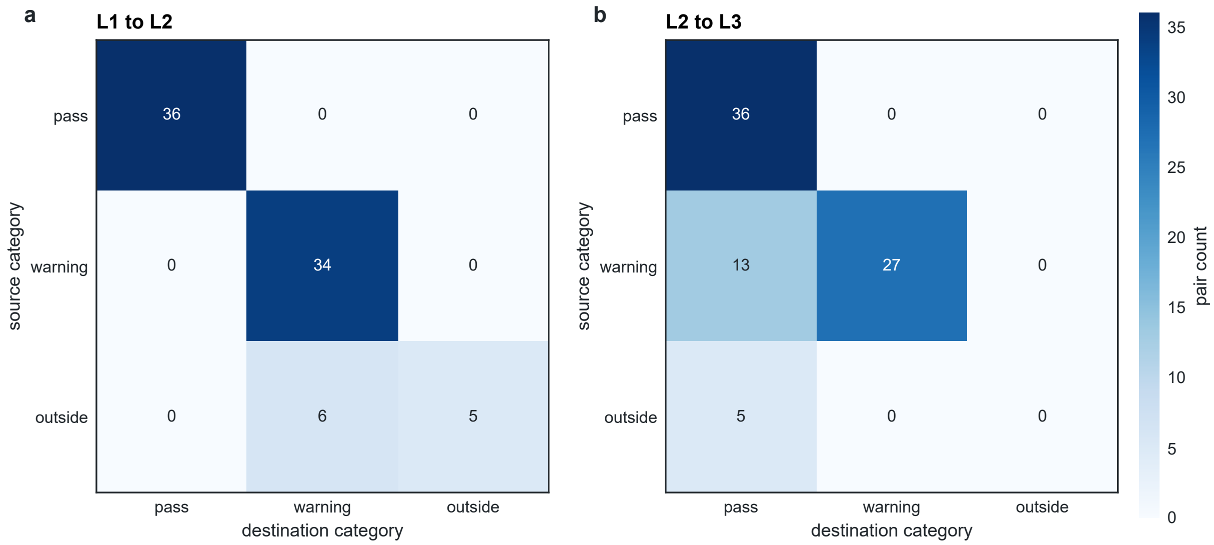

Supplementary Figure S13: Approximation-category transitions for the same 81 pairs. Rows and columns are the source and destination approximation-screening categories for L1-to-L2 and L2-to-L3 control changes. L3 converts 18 L2 warning/outside rows to pass. The transition counts describe this deliberately stratified design sample and are not transition probabilities or hardware yields.

Supplementary Table S27: Control-parameter transfer grids and interpretation. Signed grids include both signs where shown.

Axis	Grid	Interpretation boundary
dark-gap force fraction	$0, 10^{-5}, 10^{-4}, 10^{-3}, 10^{-2}$	false-ZZ shift from hidden force, separated from the zero-residual cross-window phase
AOD phase step	$0, 0.01, 0.03, 0.10, 0.30$ rad	deterministic boundary-phase perturbation
linear switching chirp	$0, \pm5, \pm10, \pm25, \pm50$ Hz/μs	linear frequency ramp within each window
edge transient chirp	$0, \pm10, \pm50, \pm100, \pm500$ Hz	integrated triangular frequency transient over rise/fall edges
residual AOD/AOM detuning	coarse -5 to $+5$ kHz; fine $0, \pm10, \pm50, \pm100, \pm250, \pm500$ Hz	compensated beat-note residual
mode-frequency drift	common $0, \pm1, \pm10, \pm50, \pm100, \pm500$ Hz; random rms $0, 1, 10, 50, 100, 500$ Hz	common grid shifts all modes equally; random grid uses 512 fixed-seed mode-resolved offset vectors
mode-resolved heating	$1, 10, 30, 100, 1000$ quanta/s per mode	$\sum_m \dot{\bar{n}}_m T$ bookkeeping only
scalar leakage	$0, 10^{-4}, 10^{-3}, 10^{-2}, 5 \times 10^{-2}$	distance-weighted scalar addressing model
directed leakage matrix	same scales, 512 fixed seeds per scale	reproducible pair-resolved asymmetry
intensity noise	$10^{-4}, 10^{-3}, 10^{-2}$ fractional rms	512 window-resolved seeded programs per level
timing jitter	1, 10, 50, 100, 500 ns rms	512 seeded switching schedules per level
boundary-phase noise	$0, 0.005, 0.01, 0.02, 0.05, 0.10$ rad rms per window	512 seeded phase programs per level
scrambled boundary phase	independent uniform phase in $[0, 2\pi)$ per active window	512 seeded phase-rule controls
scattering rate	$0.1, 1, 3, 10, 100$ s^{-1}	scanned $\Gamma_{\mathrm{sc}} T$ bookkeeping; no multilevel calculation

The 13387 individual records include every stochastic realization rather than only its mean. In the random-mode-drift axis, each seed specifies one mode-resolved offset vector at the tabulated rms scale in hertz; that vector is fixed throughout the corresponding simulated sequence. The resulting finite seeded set is treated as a declared design ensemble, not as a universal noise distribution. For each stochastic grid point, `robustness_quantile_summary.csv` reports the mean, median, sample standard deviation, p05, p50, p95, maximum sampled response, and a 95% nonparametric percentile-bootstrap interval for p95 using 2000 resamples. Quantiles use NumPy's linear sample definition. Stochastic threshold decisions use 512 realizations per grid point together with percentile-bootstrap confidence intervals, as summarized in the machine-readable threshold table. Deterministic axes use their exact sampled-grid response. These decision coordinates do not imply interpolation, probability, hardware yield, or measured tolerance.

The dark-gap axis keeps the intended target windows disjoint and bounds hidden force between windows; scalar and directed-matrix leakage instead provide residual simultaneous-forcing controls. Their separation prevents the nominal cross-window phase from being attributed to either imperfection.

Supplementary Table S28: Selected responses from the control-parameter transfer envelope. Values are model-level estimates.

Axis	scanned extreme	largest reported response
dark-gap residual force	0.01 of addressed force	$\lvert\Delta\Phi\rvert = 0.00377$ rad
AOD switching phase step	0.30 rad	$\lvert\Delta\Phi\rvert = 0.106$ rad
linear AOD chirp	± 50 Hz/μs	max $\lvert\Delta\Phi\rvert = 0.00101$ rad
edge-transient chirp	± 500 Hz	max $\lvert\Delta\Phi\rvert = 2.65 \times 10^{-6}$ rad
common mode drift	± 500 Hz	max $\lvert\Delta\Phi\rvert = 0.0225$ rad
scalar leakage	0.05	max spectator ZZ = 0.0347 rad
combined stress set	512 sampled records	27 with $\lvert\Delta\Phi\rvert < 10^{-2}$ rad; 5 with $\lvert\Delta\Phi\rvert < 10^{-3}$ rad

The combined set samples all stochastic error families jointly with fixed seeds, including boundary-phase noise. The thresholds in the last row of Table S28 apply specifically to the absolute pair-phase shift $|\Delta\Phi|$. Its threshold counts are numbers of passing records in the declared sampled ensemble, not probabilities, confidence intervals, or device yields. Heating and scattering are bookkeeping outputs, $\sum_m \dot{\bar{n}}_m T$ and $\Gamma_{\mathrm{sc}} T$, and do not alter the unitary phase trajectory in the present solver. Device-specific interpretation requires measured mode-resolved heating and a multilevel scattering calculation. The authors' reproducibility workflow generates individual, combined, and threshold CSV files, plus dedicated dark-gap, switching-phase, and mode-drift figures.

S17.2 Idealized single-projector apparatus-interface coordinates

The same individual-axis configurations are propagated through the idealized single-projector Hamiltonian without recalibrating the nominal force. The deterministic local phases are denoted λ_i and λ_j. Their robustness coordinates are

$$\Delta\lambda_q = \mathrm{wrap}_{2\pi}[\lambda_q - \lambda_q^{(0)}], \qquad \Delta\lambda_{\mathrm{RMS}} = \sqrt{\frac{(\Delta\lambda_i)^2 + (\Delta\lambda_j)^2}{2}}. \tag{S115}$$

The reported robustness values use this conventional 2π controller-phase branch; in particular, the 2.9236-rad scrambled-control entry in Table S29 is retained without reprocessing. Because $e^{i(\lambda_q+\pi)Z_q}$ differs from $e^{i\lambda_q Z_q}$ only by a global phase, a channel-equivalent minimal frame distance could instead be reduced modulo π. That additional reduction is not applied here, so $\Delta\lambda_{\mathrm{RMS}}$ is a conservative controller-coordinate drift rather than the minimal channel-equivalent distance. Thus the nominal approximately 1.35-rad local phase is a calibratable frame coordinate, not an error; only its uncompensated 2π-wrapped variation is reported as a burden. Common and subsequent-operation motion are summarized by

$$B_{\mathrm{common}} = \sum_m (2\bar{n}_m + 1)|\beta_m|^2, \qquad B_{\mathrm{next}}^{\max} = \max_{z_i, z_j = \pm 1} \sum_m (2\bar{n}_m + 1)|\beta_m + z_i\alpha_{im} + z_j\alpha_{jm}|^2. \tag{S116}$$

The source data record the real, imaginary, and absolute values of every mode-resolved β_m. For the known-Z conditional-Ramsey protocol, each record also contains C_z, $\vartheta_z^{\mathrm{mot}}$, and the coherent phasor average C_{coh} for every seeded axis/value ensemble. These are exact model-level conditional-displacement coordinates, not measured contrasts.

Supplementary Table S29: Idealized single-projector apparatus-interface summary. Extrema are over the declared grids, with units stated in the axis labels. $\Delta\lambda_{\mathrm{RMS}}$ is the conservative controller-coordinate fluctuation around the nominal local-frame calibration on the 2π branch defined in Eq. (S81); it is not the minimal channel-equivalent modulo-π distance. The nominal phase itself is not an error. The scrambled row uses independent uniform phases in $[0, 2\pi)$ for each active window.

axis	grid	max $\Delta\lambda_{\mathrm{RMS}}$ (rad)	max B_{common}	max $B^{\max}_{\mathrm{next}}$	min C_z	min C_{coh}
intensity noise (fractional rms)	$[1.00 \times 10^{-4}, 0.0100]$	0.0272	0.0026	0.0104	0.9969	0.9995
residual detuning (Hz)	$[-5.00 \times 10^{3}, 5.00 \times 10^{3}]$	0.8215	0.5458	2.1831	0.7363	0.7363
common mode drift (Hz)	$[-500.0000, 500.0000]$	0.0544	0.0071	0.0282	0.9956	0.9956
random mode drift (Hz rms)	$[0, 500.0000]$	0.1556	0.0489	0.1958	0.9704	0.9948
AOD phase step (rad)	$[0, 0.3000]$	0.3621	0.0462	0.1847	0.9688	0.9688
linear chirp (Hz/μs)	$[-50.0000, 50.0000]$	3.68×10^{-4}	1.60×10^{-4}	6.40×10^{-4}	0.9999	0.9999
edge chirp (Hz)	$[-500.0000, 500.0000]$	1.15×10^{-6}	1.56×10^{-4}	6.25×10^{-4}	0.9999	0.9999
timing jitter (μs rms)	$[0.0010, 0.5000]$	0.5502	0.0558	0.2233	0.9499	0.9911
boundary-phase noise (rad/window rms)	$[0, 0.1000]$	0.0642	0.2685	1.0741	0.7988	0.9635
scrambled boundary phase (rad/window)	uniform $[0, 2\pi)$	2.9236	23.6541	94.6162	1.32×10^{-11}	0.1204

S17.3 Fixed-frame and instance-recalibrated channels

The coherent two-qubit channel is propagated for the same deterministic grids and the same 512-seed stochastic instances used above, excluding the scrambled boundary-phase control. Let $(\lambda_i^{(0)}, \lambda_j^{(0)})$ be the effective target-frame coefficients at the zero-error point and $(\lambda_i^{(r)}, \lambda_j^{(r)})$ those inferred for perturbation instance r. The instance-recalibrated channel applies $[-\lambda_i^{(r)}, -\lambda_j^{(r)}]$, while the fixed-frame channel applies $[-\lambda_i^{(0)}, -\lambda_j^{(0)}]$ for every r. Thus their difference is an experimentally relevant virtual-frame stability requirement rather than a change to the force trajectory.

For each stochastic grid point, individual Choi matrices are averaged before ensemble-channel metrics are evaluated. Per-instance p05, median, p95, sampled maxima, and percentile-bootstrap intervals for p95 are recorded separately. The representative results are

Supplementary Table S30: Fixed-frame and recalibrated coherent channel coordinates. Stochastic rows report p05 average fidelity and deterministic rows the exact grid value; the final column is the sampled p95 local-frame drift.

axis	grid value	fixed nominal frame	instance recalibrated	p95 $\Delta\lambda_{\mathrm{RMS}}$ (rad)
AOD phase step (rad)	0.30	0.803458	0.988002	0.362
timing jitter (μs)	0.5	0.777430	0.985109	0.393
boundary-phase noise (rad/window)	0.1	0.941410	0.943236	0.0412
combined sampled stress	1	0.409104	0.551954	1.12

The combined sampled set gives Choi-ensemble average fidelities 0.768359 and 0.907551 for the fixed and recalibrated policies, respectively. These are coherent reduced-channel quantities. Scattering probability and heating increments are reported as independent bookkeeping columns; neither is embedded in the CPTP map because no corresponding open-system channel has been specified.

S18. Source Data and Reproducibility

S18.1 Source data and code availability

The equations, parameter tables, plotted summaries, and numerical validation results needed to assess the claims are contained in the main text and this Supplementary Information. Source data and code supporting this study are available from the corresponding authors upon reasonable request. The calculations were produced in the authors' working reproducibility tree, which comprises Python source, shared YAML configuration, LaTeX source, plotted CSV files, cached publication data, and machine-readable provenance.

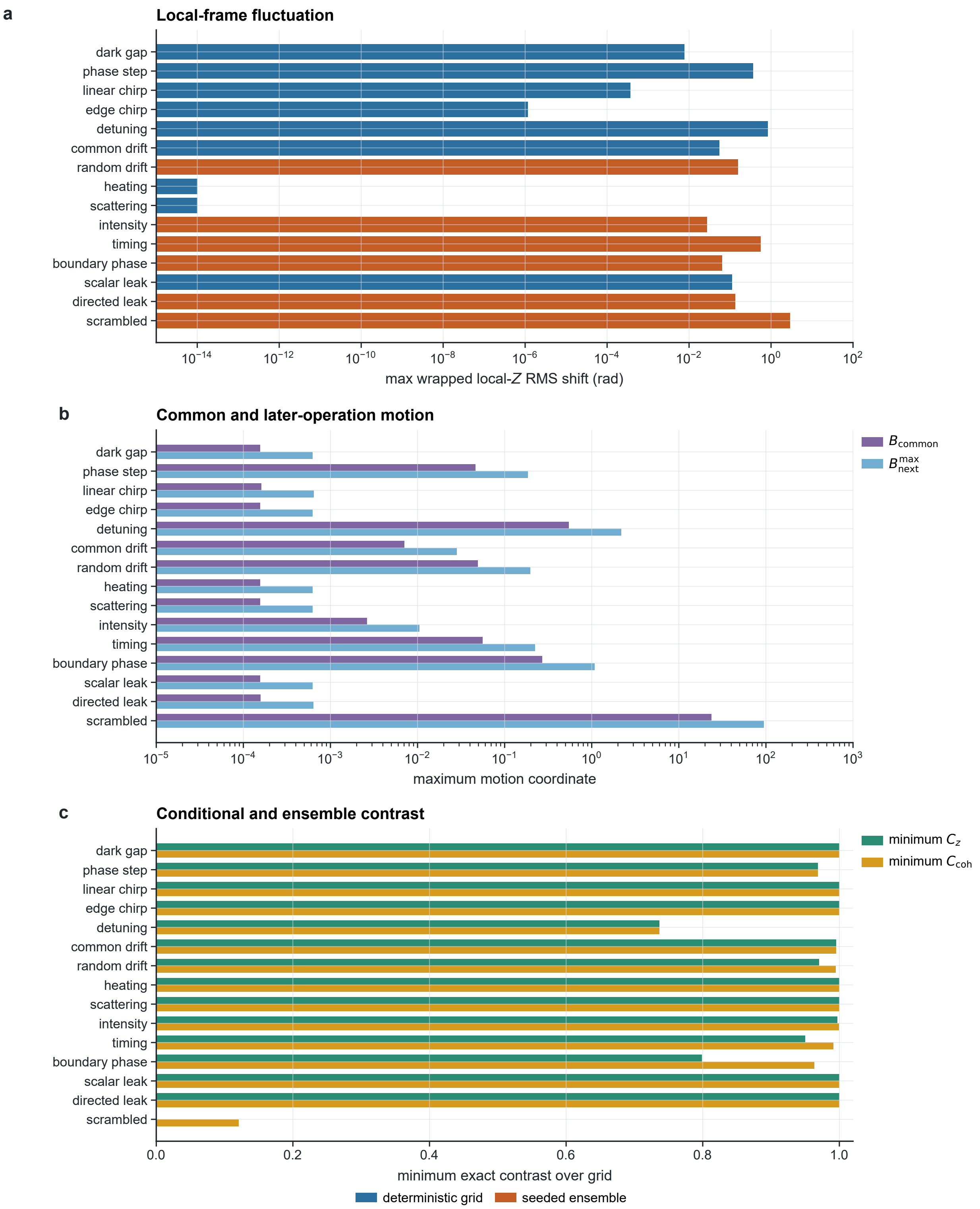

Supplementary Figure S14: Idealized single-projector local-phase, common-motion, and conditional-contrast coordinates. (a) Maximum 2π-wrapped local-Z controller-coordinate RMS fluctuation relative to the fixed nominal calibration. (b) Common and worst target-branch absolute-motion coordinates. (c) Minimum exact branch contrast and coherent-ensemble contrast over each declared axis grid. Deterministic axes use exact grid extrema. Stochastic axes use 512 seeds per grid point from the fixed 30000 (random drift), 50000 (intensity), 70000 (timing), 90000 (directed leakage), 110000 (boundary phase), and 150000 (scrambled phase) families. The bars show sampled extrema, not p95 estimates; the authors' working reproducibility tree records linear p05/p50/p95 values and 95% percentile-bootstrap intervals for p95 with 2000 resamples under the internal filename `data/robustness_quantile_summary.csv`. The deterministic nominal local phase is not plotted as an error, and none of the coordinates is a measured apparatus tolerance or fidelity.

S18.2 Reproduction modes

Within that working tree, the top-level command is

```
python reproduce_all.py --mode cached
```

which rebuilds figures from the publication CSV files, reruns the numerical consistency checks, compiles both PDFs with `latexmk`, and writes a concise reproduction summary. The `quick` mode is a smoke test that does not replace publication data, and the `full` mode recomputes the publication CSV set before rebuilding the PDFs. This command documents the internal workflow used to generate and validate the reported results.

S18.3 Dataset and generator map

In the authors' working tree, each plotted CSV is linked to its generator, configuration, model label, and range of interpretation. Stochastic calculations use fixed seeds, and the runtime environment is recorded during reproduction. The internal README and machine-readable manifests record file inventories, hashes, commands, software packages, and seed definitions. These materials are covered by the availability statement in Section S18.1.

S18.4 Scope of numerical reproducibility

These checks establish numerical consistency within the reduced-force and projector-force models. They do not constitute experimental validation or supply apparatus parameters that are absent from the model inputs.

References

[1] Baldwin, C.H., Bjork, B.J., Foss-Feig, M., Gaebler, J.P., Hayes, D., Kokish, M.G., Langer, C., Sedlacek, J.A., Stack, D., Vittorini, G.: High-fidelity light-shift gate for clock-state qubits. Physical Review A **103**, 012603 (2021) `https://doi.org/10.1103/PhysRevA.103.012603` arXiv:2003.01102 [quant-ph]

[2] Hou, Y.-H., Yi, Y.-J., Wu, Y.-K., Chen, Y.-Y., Zhang, L., Wang, Y., Xu, Y.-L., Zhang, C., Mei, Q.-X., Yang, H.-X., Ma, J.-Y., Guo, S.-A., Ye, J., Qi, B.-X., Zhou, Z.-C., Hou, P.-Y., Duan, L.-M.: Individually addressed entangling gates in a two-dimensional ion crystal. Nature Communications **15**, 9710 (2024) `https://doi.org/10.1038/s41467-024-53405-z`